Role of Intermetallic Phases in Corrosion Initiation

of AA5083 and AA6082 Aluminium Alloys

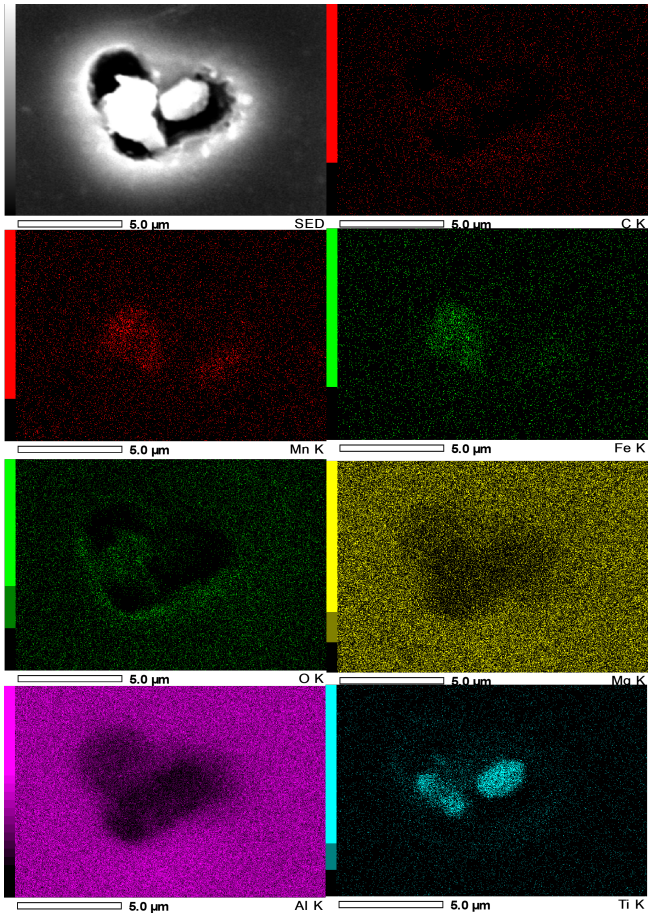

ROLE OF INTERMETALLIC PHASES IN CORROSION INITIATION

OF AA5083 AND AA6082 ALUMINIUM ALLOYS

Submitted by

Vinod GANESH

to obtain the degree of Master of Science
at the Delft University of Technology

Student Number: 5247594

Thesis Committee:

Prof. Dr. Yaiza Gonzalez-Garcia, Technische Universiteit Delft

Dr. Cristina Petcu, ASML Holding N.V.

Dr. Ehsan Rahimi, Technische Universiteit Delft

Prof. Dr. Peyman Taheri, Technische Universiteit Delft

Prof. Dr. Jie Zhou, Technische Universiteit Delft

TU Delft Delft University of Technology

ASML

Keywords: Intermetallic phases, Localised corrosion, Corrosion initiation, AFM-SKPFM, In-situ SECM, Aluminium alloys.

Front & Back: The picture in the cover is a SEM-EDX image of Ti intermetallic particle forming a trench where the Aluminium base matrix is corroding.

An electronic version of this dissertation is available at
http://repository.tudelft.nl/.

CONTENTS

List of Figures

LIST OF TABLES

ABSTRACT

Many applications requiring light weight, good strength and corrosion resistance use 5xxx and 6xxx series of aluminium alloys. One such application is for cooling channels in ASML cooling systems where AA5083 and AA6082 Cu-free alloys are employed to carry the flow of semiconductor-grade ultra-pure water. Due to several reasons, even in ultra-pure water condition, corrosion of aluminium channels is unavoidable. Localised corrosion due to the galvanic coupling formed between the intermetallic phase and the aluminium matrix is known to be the reason behind the corrosion initiation and propagation. However, the behaviour and role of different types of intermetallic phases are not completely understood. This study attempts to understand better the role of intermetallic phases on the corrosion initiation of A5083 and AA6082 alloys. For this purpose, this study employs localised techniques to evaluate the electrochemical property of intermetallic phases and to study the activity of the sample surface through SKPFM and in-situ SECM experiments, respectively. The study also performs potentiodynamic polarisation tests to understand the overall corrosion performance of the alloys in ultra-pure water, an artificial mix of impure water and 0.1 M NaCl solution. In addition, the electrochemical behaviour of the intermetallic phases, it is found that the alloy composition and the surface distribution of the intermetallic phases also contributes and have significant effect on the localised corrosion initiation. The results of localised techniques carried out using 0.1 M NaCl solution agree with the observations obtained for ultra-pure water and the artificial mixture conditions.

1

INTRODUCTION

1.1. CORROSION AND ITS IMPACTS

Corrosion of metals is a very common phenomenon where the metal reacts with the environment to form metal oxides. R. Winston Revie and Herbert H. Uhlig in their book *Corrosion and Corrosion Control* [1] defines corrosion as a chemical or electrochemical attack on metals by its environment. Although there are several ways to define corrosion, I see this phenomenon as nature's play where nature gets back what it had initially in the form that it likes i.e. converting back to metal-oxides from where humans extracted the metals from.

As the utilization of metals and metallic structures are the sole need for industrial and infrastructural developments, corrosion is inevitably one of the most expensive problems to deal with [1, 2]. Apart from impacting economically, unmonitored corrosion leads to severe safety issues. The unfortunate yet famous incidents like the recent collapse of Morandi Bridge in Genoa, Italy, the disaster of a chemical plant in Bhopal, India in 1984 and many more act as an alarming reminder on how deathly the effects of corrosion can be [3, 4].

Knowing that corrosion is an inevitable phenomenon, several industries and research organisations are investing to gain knowledge on the reason behind corrosion and finding ways to minimize the effect of corrosion, to improve the lifetime of the material and in turn reducing the costs associated with it. This project is one such attempt to understand the reason behind the corrosion initiation of aluminium (Al) alloys.

1.2. PROJECT MOTIVATION

ASML Holding N.V. is a company situated in Veldhoven, the Netherlands which manufactures lithography machines for printing Integrated Circuit (IC) chips. Their DUV (Deep Ultra-Violet) systems and EUV (Extreme Ultra-Violet) systems with the use of ultraviolet beams helps to print complex transistors and chip architectures. The EUV sys-

tems are very unique to ASML and it helps push the Moore's law [5] forward by enabling chip manufacturers to fit more number of transistors per unit area.

Water cooling system of these lithography machines consist of complex channel architecture throughout and around the necessary parts of the machine. The metal channels are mostly made of Stainless Steel and Al alloys of type AA5083 and AA6082. These cooling system in ASML lithography machines runs Ultra Pure Water (UPW) specified by the ASTM D5127-13 [6] standard as the coolant. Due to its ease of access in electronic industry and low conductivity causing low corrosion damage to the channels [7, 8], UPW are very much preferred for this purpose.

Even by utilising UPW as coolant, the company found that the channels, especially those made of Al alloys, face severe localised corrosion after certain period of usage. The contamination of UPW by few ion types caused due to material dissolution from the channels as a result of corrosion after 4 years in use is tabulated in table 1.1. From this data, it can be proved that the corrosion is happening in the channels and at some point in future, corrosion is expected to cause bigger damages.

Table 1.1: Range of contamination of various ion types in UPW in parts per million (ppm)

Ion Type	Mg	Cu	Al	Si	Na	Cl
UPW	-	-	-	-	-	-
Contaminated UPW	0.01 - 0.5	0.02 - 7	0.003 - 155	0.2 - 6	0.03 - 5	0.05 - 5

As an high-tech industry, ASML cannot afford to damage critical parts of the lithography system due to external corrosion damage in cooling channels. Further, damages occurred while production at customer site would lead to a sever increase in lead time due to repair and in turn the associated costs. Hence, ASML is trying to find the right solution by understanding the corrosion mechanism and also in finding methods to inhibit corrosion. This Master's thesis project is one of the contributions in understanding the corrosion mechanism of Al AA5083 and AA6082 alloys happened as a result of collaboration with Technische Universiteit Delft (TU Delft) and ASML.

This master's thesis aims to understand the role of intermetallic particles in corrosion initiation of AA5083 and AA6082 Al alloys. The unique feature of this project is the utilisation of wide variety of corrosion analysis methods starting from accelerated electrochemical corrosion analysis, Kelvin probe microscopy to Scanning Electrochemical Microscopy techniques, to understand and analyse the factors that influence the corrosion initiation in these alloys.

The following chapter 2 summarises the literature knowledge related to the topic which is already available. Chapter 3 explains the materials and methodology used in this study followed by results and discussions in chapters 4. Following this, conclusions and future recommendations are summarised in the final chapter - chapter 5.

2

LITERATURE SURVEY

2.1. ALUMINIUM ALLOYS AND ITS INTERMETALLIC PHASES

Aluminium (Al) alloys are most preferred alloys for engineering applications requiring high strength to weight ratio [9]. Transport industries gains a tremendous advantage from utilising Al alloys as its low density and high strength to weight ratio helps in reducing the vehicle weight and in turn the associated emissions [10–12].

Al alloys are classified into various series starting from 1XXX until 9XXX based on its alloying elements. The table 2.1 lists the various Al alloy series and its main alloying elements. The quantity and type of alloying elements plays an important role in determining the end properties of the alloy. Depending on the requirements for a specific application, the alloy constituents and composition is modified to fit the application.

Table 2.1: Aluminium Alloy series and its corresponding alloying element(s). (Adapted from [13])

Aluminium Alloy Series	Main Alloying element(s)
1XXX	Predominantly Pure Aluminium
2XXX	Copper
3XXX	Manganese
4XXX	Silicon
5XXX	Magnesium
6XXX	Magnesium and Silicon
7XXX	Zinc
8XXX	Other elements like Lithium
9XXX	Unassigned

These series of Al alloys are further grouped into heat treatable and non-heat treatable alloys. Having said that the end properties are mainly dependent on the alloying elements, the end properties can be further tuned by different hardening processes. The

heat treatable alloys are susceptible to micro-structure and property change during age hardening process whereas for non-heat treatable alloys, age hardening would not have any significant effect. Hence, non-heat treatable alloys are hardened by plastic deformation know as strain hardening. 2XXX, 3XXX and 7XXX series of Al alloys generally categorised under heat treatable category and 1XXX, 4XXX and 8XXX are under non-heat treatable category.

Intermetallic Phases (IMPs) are secondary phases which are formed due to the presence of alloying elements and other impurities in the alloy matrix. The composition of the alloying elements also determine the type, size and shape of IMPs that can form in the alloy matrix. Depending on the type and morphology of the IMPs, the end properties of the alloy could turn out to be either beneficial or detrimental. The table 2.2 lists the common IMPs formed in each Al alloy series.

S. Ji et. al [14] studies the effect of Iron (Fe) content on Al-Mg-Si-Mn and Al-Mg-Si alloys acts as a good example how the alloy content affects the IMP formation and hence affecting the mechanical properties. The study shows an increasing and decreasing trend for strength and ductility respectively as the Fe content is increased up to 0.5 $wt\%$ whereas further increase in Fe content resulted in significant lowering of ultimate strength. Formation of needle like morphology of $\beta - AlFe$ when Fe content is increased is reported to be the reason behind this behaviour.

Table 2.2: Aluminium Alloy series and IMC formed in it. (Adapted from [13])

Aluminium Alloy Series	Main Alloying Elements	Typical IMCs formed
1XXX	Predominantly Pure Aluminium	Al_3Fe, Al_6Fe, $AlFeSi$
2XXX	Copper	Al_2Cu, Al_2CuMg, Al_7Cu_2Fe, $Al_6(CuFeMn)$
3XXX	Manganese	Al_6Mn, $Al_6(MnFe)$, $Al(MnFe)Si$
4XXX	Silicon	$Al_6(Fe,Mn)$, Al_3Mg_2, Al_8Mg_5
5XXX	Magnesium	$Al_6(Fe,Mn)$, Al_3Mg_2, Al_8Mg_5
6XXX	Magnesium and Silicon	Mg_2Si, Al_2Cu, $AlSiMnFe$, $AlMgSi$, Al_3Fe
7XXX	Zinc	$MgZn_2$, $Al_{12}CrMn$, $(Fe,Cr)_3SiAl_12$, $Al_{23}CuFe_4$, $Mg(ZnAlCu_2)$, Al_7Cu_2Fe, Al_3Fe
8XXX	Other elements like Lithium	Al_2CuLi, Al_7Cu_2Fe, Al_2CuFe, Al_3Fe

Knowing that the right IMPs are necessary to improve the mechanical properties of the alloy, they are equally know to cause localised corrosion in the alloy matrix. Localised corrosion occurs due to the difference in electrochemical potential between the IMP and the alloy matrix. The difference in electrochemical potential creates local galvanic coupling leading to localised material dissolution from the anodic site. Depending on the type and the constitution, IMPs can be anodic or cathodic with respect to the alloy matrix [15]. Refer to the table 2.3 that lists the electrochemical potential of different IMPs found in Al alloys.

Table 2.3: Intermetallic phases and its corresponding corrosion potential (mV Vs. SCE)(mV_{SCE}) in 0.01M NaCl solution (Adapted from [15])

Stoichiometry	Corrosion Potential (mV_{SCE})
Al_3Fe	-493
Al_2Cu	-592
Al_3Zr	-752
Al_6Mn	-839
Al_3Ti	-620
Mg_2Al_3	-1124
Mg_2Si	-1355
Al_7Cu_2Fe	-549
$Mg(AlCu)$	-898
Al_2CuMg	-956
$Al_{20}Cu_2Mn_3$	-550
$Al_{12}Mn_3Si$	-890
Al (99.9999)	-679
Cu (99.9)	-177
Si (99.9995)	-450
Mg (99.9)	-1601
Mn (99.9)	-1315
Cr (99.0)	-495
Zn (99.9)	-985

The IMPs that are anodic with respect to the alloy matrix tend to dissolve themselves or selectively dissolve the most anodic substance within themselves creating localised corrosion whereas the IMPs that are cathodic will dissolve the anodic alloy matrix forming a trench around the IMP along with selectively dissolving the most anodic element within them. More information on de-alloying and trenching due to IMP activity can be found from the studies of A. Kosari et. al [16, 17]. Figure 2.1 shows the Scanning Tunneling Electron Microscopy (STEM) image of formation of trench around the $\theta - Al_2Cu$ phase, know to be cathodic to the base Al matrix (refer to table 2.3), found in aerospace aluminium alloys (2XXX series). Further, bright spots on the IMP can be found in figure 2.1(a) which is associated with the de-alloying of the phase where aluminium being the most anoic substance in $\theta - Al_2Cu$ phase, is selectively dissolved from it.

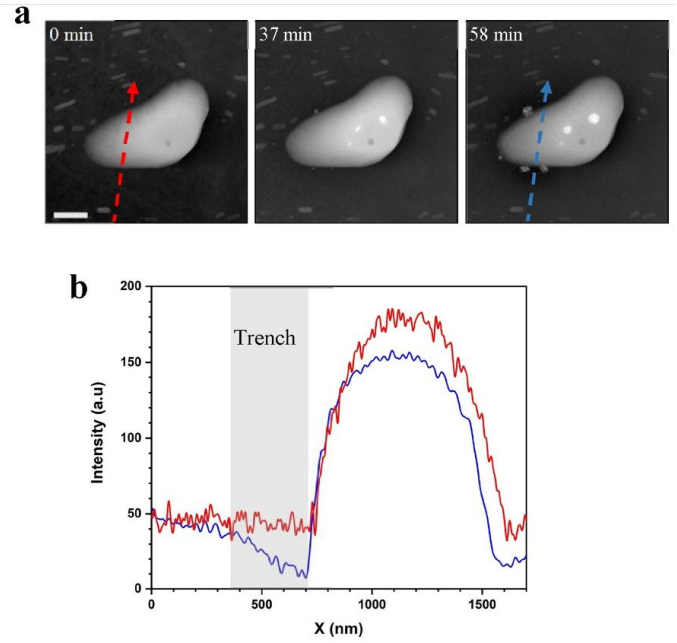

Figure 2.1: (a) STEM image of $\theta - Al_2Cu$ phase showing contrast change indicating material dissolution around the IMP with respect to time. (b) Line profile of across the IMP indicating trenching at 58 min of immersion in 0.01M NaCl solution. The scale bar length corresponds to 500 nm. [16])

2.2. PITTING CORROSION IN ALUMINIUM ALLOYS

2.2.1. ALUMINIUM PASSIVE LAYER

Pure aluminium is regarded as one of the most active metals having a reduction potential of -1.66 V (vs. SHE), due to which, at neutral pH conditions Al readily forms a passive film on its exposed surface to protect it from corrosion damages [18, 19]. The effectiveness of the passive layer protection against corrosion depends on factors like the exposed environment and pH.

Figure 2.2 shows the Pourbaix diagram of pure Al in water at 298K where it can be clearly seen that the stability of oxide layer (Al_2O_3) is restricted to pH values between 4 and 9. At lower end of pH (below 4) the aluminium dissolves as aluminium ions (Al^{3+}) and at very high end of pH (above 9), the aluminium dissolves as AlO^{2-} ions denoting that no protective oxide layer is formed and hence, the base metal undergoes a severe corrosion.

Even within the stable pH range for oxide layer formation, the thin layer is not formed uniformly over the surface. The presence of IMPs, defects and many other surface factors tend to weaken the passive layer locally around the specific spot [18]. This provides a easy pass way for corrosive ions like Cl^- to break open the layer at its weak point and initiate localised corrosion [13].

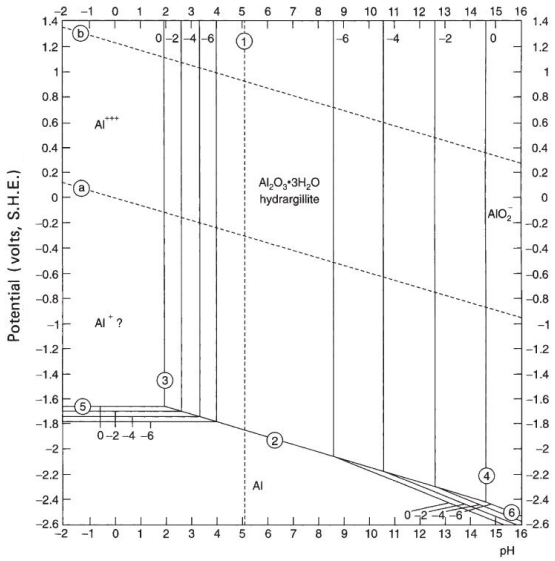

Figure 2.2: Pourbaix diagram for Pure Aluminium in water at 298 K. [20]

2.2.2. PITTING CORROSION

Pitting corrosion is a very common phenomenon occurring in stainless steels, nickel and aluminium alloys [21–23]. These alloys are susceptible to pitting type corrosion when there is a presence of very corrosive ions like chlorides (Cl^-) [24]. Cl^- ions can be very aggressive in penetrating through the metal due to its small radius of 18.1 nm [25]. The penetration through the metal and formation of pits follows three major steps:

- Pitting Initiation
- Passive Layer Breakdown
- Pitting Propagation

Pitting is initiated by the chloride ions which gets attracted towards the surface due the positive charge of Al surface. The Cl^- ions eventually penetrates through the oxide layer by break opening the weaker or thin sections of oxide layer which are formed on top of surface attributes like impurities, IMPs, surface scratches and many more. As the penetration of Cl^- ions breaking the passive layer begins, the surrounding electrolyte also flows into the initiated pit and constantly supplies water and oxygen to keep the pit growing.

After the pit gets initiated, it either gets passivated, becomes meta-stable or propagates into a stable pit. Occurrence of pitting can be characterised by sudden increase of current (density) in a typical potentiodynamic polarisation test and the potential where it happens is denoted as pitting potential (E_{pit}). Meta-stable pitting is activation and

passivation of pits in a very short period of time and it occurs just below the pitting potential (E_{pit}) [26].

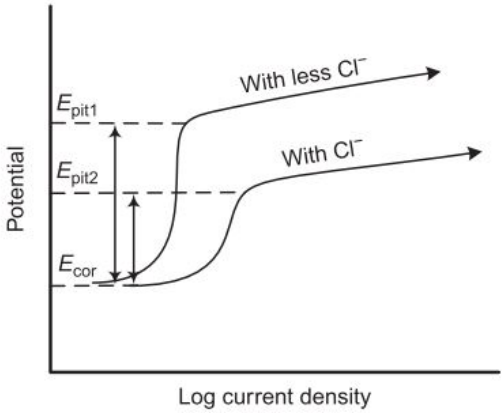

Figure 2.3: Representation of Potentiodynamic polarisation plot showing pitting and pitting potential in the anodic branch (Adapted from [13])

Some of the meta-stable pits grows and propogates into a stable pit at pitting potential where the corrosion follows the mechanism of anodic dissolution of Al matrix [26, 27]. Figure 2.3 shows a schematic representation of the anodic branch of potentiodynamic polarisation curve where a sudden increase in current is observed at E_{pit} denoting stable pitting. The resistance of an material to pitting is denoted by the difference in corrosion potential (E_{cor}) and the pitting potential (E_{pit}) where if the difference is higher, higher the resistance to pitting.

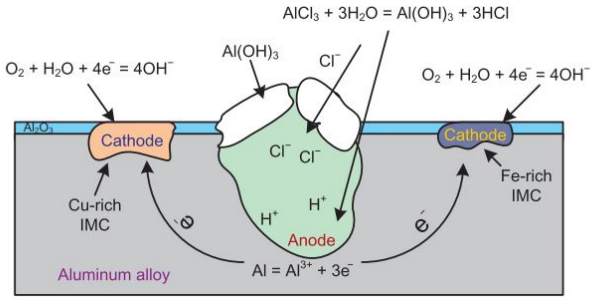

Figure 2.4: Schematic representation of pitting corrosion in Aluminium alloys (Adapted from [13])

Figure 2.4 shows a schematic of the anodic and cathodic reactions happening while pitting process. In localised corrosion scenario, aluminium ions attract chloride ions

in the presence of water to form aluminium hydroxide and hydrochloric acid. The formation of acid reduces the pH inside the pit which further increases the dissolution of aluminium. The hydroxides of aluminium formed will settle on top of the surface acting as a cover to the pit. Although the pit is covered by hydroxides (see figure 2.4), the corrosion will still happens underneath the cover and material degradation happens leading to mechanical failures. Further, the hydroxide cover is porous in nature due to which the chloride ions can easily enter the pit fueling the pitting process [13].

2.3. MICROSTRUCTURE OF AA5083 AND AA6082 ALLOYS

2.3.1. MICROSTRUCTURE AND INTERMETALLIC PHASES OF AA5083

Al-Mg alloys are non-heat treatable and are strengthened through solid solution strengthening by adding magnesium (Mg) and through cold working processes [28, 29]. The general composition of AA5083 alloy consist of alloying elements like magnesium (Mg), silicon (Si), manganese (Mn) and iron (Fe). Apart from these major constituents traces of titanium (Ti), zinc (Zn) and other elements are also found. Mn, Ti and chromium (Cr) are added to Al-Mg alloys to further increase their strength by preventing grain growth. The table 2.4 gives the chemical composition in weight percentage of commercially available AA5082 alloys.

Table 2.4: Elemental composition of AA5083 Alloy in wt% where Al being the major constituent (Adapted from [30]).

Al Alloy	Mg	Si	Mn	Fe	Cr	Ti	Cu	Zn	Others
5083	4.0-4.9	0.4	0.4-1.0	0.4	0.05-0.25	0.15	0.1	0.25	0.15

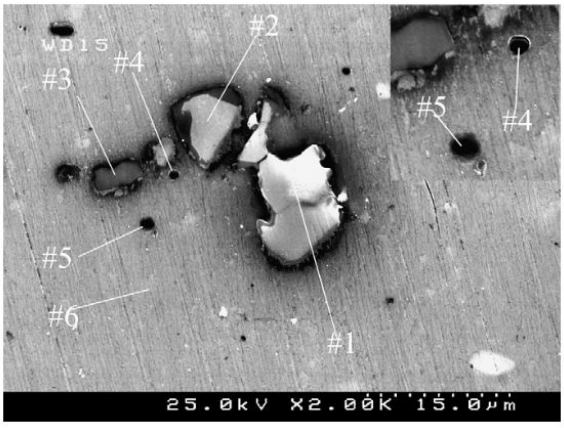

Figure 2.5: SEM image of $Al-(Si,Mn,Fe,Cr)$ (bright feature) and Mg_2Si (dark spots) intermetallic phases present in AA5083 alloy (Adapted from [31])

K.A. Yasakau et al. [31] mentioned four major types of IMPs found in Al-Mg alloys, which are, Al_6MnFe, $Al-(Si,Mn,Fe,Cr)$, Mg_2Si and Al_3Mg_2 phases. Through mi-

crostructure examination via Scanning Electron Microscopy (SEM), the areas of dark fields usually correspond to Mg_2Si IMP whereas the bright areas correspond to Fe-rich IMPs such as Al_6MnFe and $Al-(Si,Mn,Fe,Cr)$ [31, 32]. The figure 2.5 shows a SEM image of AA5083 alloy after immersion in 5 mM NaCl solution for 2 hours. The markings 1, 2 and 3 corresponds to Fe-rich IMPs where 1 and 2 has composition similar to $Al-(Si,Mn,Fe,Cr)$ IMP whereas 3 has the composition of Al_6MnFe. The dark spots appearing in figure 2.5 denoted by 4 and 5 were examined to correspond to Mg_2Si IMPs. The marking 6 corresponds to the aluminium alloy matrix. U. Donatus et al. [33] mentioned that the abundance and the size of the IMPs in the matrix decreases as: Fe-Rich IMPs > Mg_2Si > β phases.

Although the study by K.A. Yasakau et al. ([31]) analysed the corrosion influence of various IMPs in detail, it failed to mention about the presence of β phase. There might be two reasons for not studying the β phase; one, the β phase might not be detected by the type of characterisation carried out due to its existence in nm size range and two, there might not be any β phase existed in the alloy examined as the β phase segregation happens after sensitization treatment as mentioned in [33].

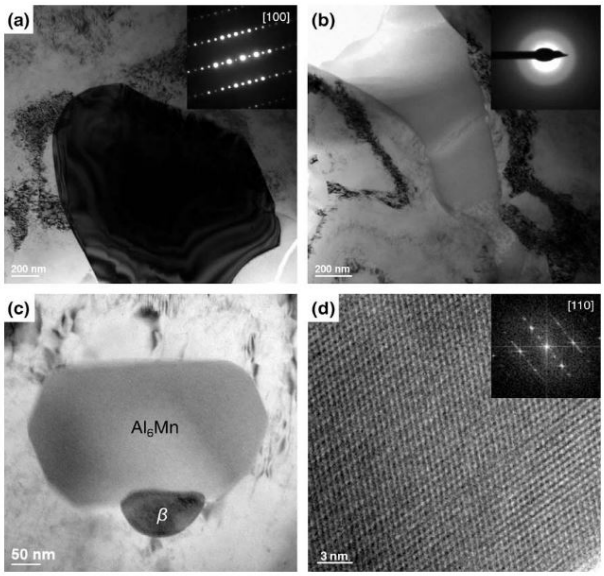

Figure 2.6: TEM images of IMPs present in AA5083 alloy. (a) $Al_{13}Fe_4$, (b) Mg_2Si, (c) Al_6Mn and β and (d) High resolution of Al_6Mn (Adapted from [34])

L. Tan and T.R. Alle [34] reported four major IMPs and additionally the presence of βAl_3Mg_2 after sensitization treatment using SEM and Transmission Electron Microscopy (TEM) techniques. The four major IMPsare mentioned to be Al_6MnFe, $Al-(Si,Mn,Fe,Cr)$, Mg_2Si and $Al_{13}Fe_4$ which are detectable easily due to its large size unike β phase. The

figure 2.6 shows the TEM images of these IMPs. Figure 2.6(a) and 2.6(b) shows the $Al_{13}Fe_4$ intermetallic phase which was found to have additional Cu and Fe preciptates, and the amorphous Mg_2Si phase respectively.

Two sizes of Al_6Mn IMPs were mentioned to be present in AA5083 alloy. One of which have 1:2 width to length ratio and the other is elongated in one direction which is mentioned to contain Fe in it. The β phase being very small in size, it is difficult to capture through SEM technique. According to Mary et. al [30] and [35] the preference of β phase nucleation follows the order of first in grain boundaries, at second phase particles, dislocations and then through bulk matrix. In addition to this claim, β phase can also be seen precipitating between the Al_6Mn intermetallic phase and the Al matrix apart from the grain boundaries. Figure 2.6(c) shows the Al_6Mn intermetallic with an attached β phase formed between the Al_6Mn intermetallic phase and the Al matrix. Figure 2.6(d) shows a high resolution image of Al_6Mn intermetallic phase.

2.3.2. MICROSTRUCTURE AND INTERMETALLIC PHASES OF AA6082

Al-Mg-Si alloys are heat-treatable aluminium alloys that are used for high strength applications requiring good corrosion resistance. In comparison with 5XXX alloys, the formation of βAl_3Mg_2 is suppressed in the 6XXX alloy series due to the addition of excess silicon. The excess silicon addition combines with magnesium and is favourable of forming Mg_2Si particle than precipitating as βAl_3Mg_2 phase [36, 37]. By this addition, it is also said to reduce the severity of intergranular corrosion (IGC) and intergranular corrosion cracking (IGCC) that occurs in 5XXX alloys [13, 38]. These series of alloys are strengthened via heat treatments like ageing process to precipitate Mg_2Si particles. The common constituents of commercially available Al-Mg-Si alloys are Mg, Si, Cu, Mn and Fe with some additions of Cr, Zn and Ti. This literature study is carried out focusing on the Cu-free Al-Mg-Si series alloy - AA6082. The chemical composition in weight percentage of commercially available AA6082 alloy is given in the table 2.5.

Table 2.5: Elemental composition of AA6082 Alloy in wt% (Adapted from [39])

Al Alloy	Si	Fe	Cu	Mn	Mg	Cr	Zn	Ti	Others
6082	0.7-1.3	0.5	0.1	0.4-1.0	0.6-1.2	0.25	0.20	0.10	0.15

The most common types of IMPs present in AA6082 alloys are to be $Al(Fe,Mn,Si)$ and Mg_2Si phases [33, 40, 41]. U. Donatus et al. [33] in their TEM study on AA6082 rich side of dissimilar friction stir weld of AA5083 and AA6082 alloy revealed various morphology of the $Al(Fe,Mn,Si)$ and Mg_2Si phases (see figure 2.7). Figure 2.7(a) and (c) shows the presence densely and less densely precipitation of $Mg-Si$ phase respectively. Figure 2.7(d) also represents the less densely precipitation of $Mg-Si$ phase.

In the presence of less dense $Mg-Si$ phase, widened precipitate free zones (PFZ) were found which helped in revealing the mechanism of intergranular corrosion. Figure 2.7(b) shows a rod like precipitate of $Al(Fe,Mn,Si)$ phase and figure 2.7(e) and (f) shows globular forms of $Mg-Si$ phase. The $Al(Fe,Mn,Si)$ phase was found to be more abundant and large in size compared to $Mg-Si$ phase. Due to the large size of $Al(Fe,Mn,Si)$

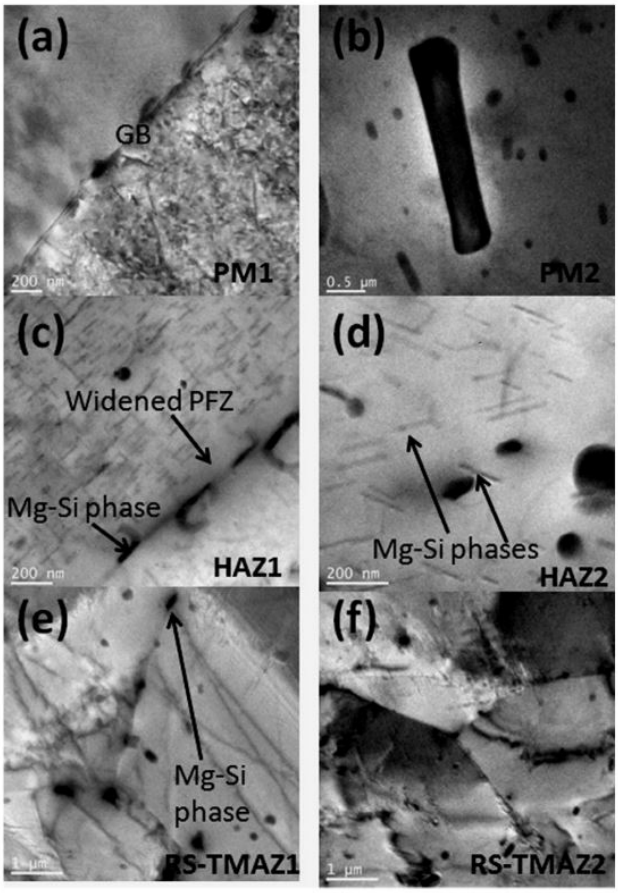

Figure 2.7: TEM images of IMPs present in AA6082 alloy. (a) densely formed $Mg-Si$, (b) $Al(Fe,Mn,Si)$ (c) and (d) Less densely formed $Mg-Si$, (e) and (f) globular $Mg-Si$ (Adapted from [33])

phase, large cavities are formed on the alloy matrix after corrosion.

Chen et. al. [41] mentioned the presence of two different morphology of iron rich $AlFeSi$ phase - α and β types. The $\alpha AlFeSi$ IMP exhibits spherical shape whereas the $\beta AlFeSi$ phase exhibits needle-like morphology. The presence of β phase is said to promote severe pitting when exposed to chloride containing environment whereas the α phase has lower tendency to promote pitting. Al-Mg-Si alloys are subjected to homogenisation treatments before any practical use in order to transform the existing β phases in as-cast alloy to α phase. However, complete transformation cannot be achieved by homogenisation treatments.

2.4. EFFECT OF INTERMETALLIC PHASES ON CORROSION INITIATION

The IMPs present in a metal matrix act cathodic or anodic with respect to the matrix. The intermetallic phases which are nobler (i.e. cathodic) with respect to the matrix, will promote the corrosion or dissolution of the base matrix. Whereas, the ones that are anodic will corrode itself. Figure 2.8 represents the reduction potential (mV vs SCE) of IMPs present in AA5XXX alloy with the dotted line denoting the potential of the aluminium matrix.

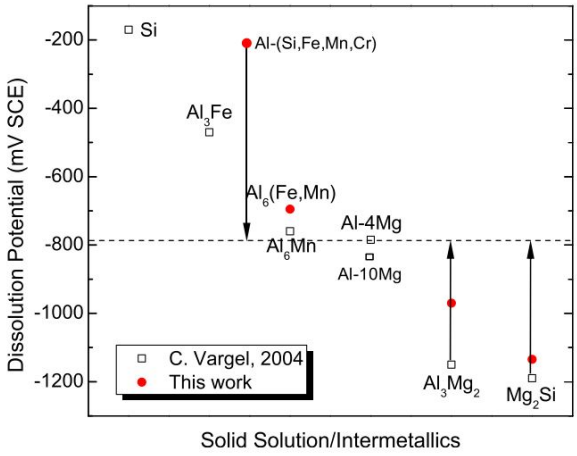

Figure 2.8: Reduction potential of intermetallic phases present in AA5083 alloy. The red markings belongs to the work of L. Tan and T.R. Allen [34]) and the square markings are from the work of C. Vargel [39]

From the figure 2.8, one can observe that the intermetallic phases containing Fe tend to be nobler whereas the ones with Mg tends to be more negative than the base metal. This correlates with the fact that Fe being more nobler than Al and Al being more nobler than Mg.Due to the scope of this project, in this section, only the relevant Fe-rich IMPs and $Mg-Si$ IMPs are considered, analysed and reported.

2.4.1. LOCALISED CORROSION IN AA5083

Several studies have supported that the formation of pit occurred around the Fe-rich (cathodic) IMPs (see figure 2.5 around marking 1) by the dissolution of Al-matrix due to the difference in electrochemical potential between them [31, 33, 42–45]. However, L. Tan and T.R. Allen [34] mentioned that $Al(Si,Fe,Mn,Cr)$ is responsible in prompting pitting but $Al_6(Fe,Mn)$ and Al_6Mn do not contribute in pitting in the thermo-mechanically treated alloy due to its similar electrochemical potential to Al-matrix. The authors further mentioned a case where $Al_6(Fe,Mn)$ arrests the corrosion attack in grain boundary after nitric acid mass loss test. The figure 2.9 shows $Al_6(Fe,Mn)$ formed in the grain

boundary arresting the corrosion along the grain boundary.

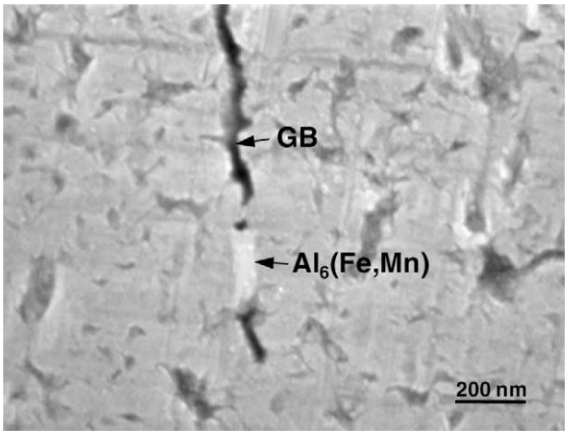

Figure 2.9: TEM images of intermetallic phases present in AA5083 alloy. (a) $Al_{13}Fe_4$, (b) Mg_2Si, (c) Al_6Mn and β and (d) High resolution of Al_6Mn (Adapted from [34])

K.A. Yasakau et al. [31] mentioned that the preferential dissolution of Al near the IMP is also due to the presence of comparatively weaker native oxide film on and around the phase. The Scanning Kelvin Probe Force Microscopy (SKPFM) analysis of immersion test carried out by the author revealed an increase in potential difference between matrix and the Fe-rich phase after immersion. It is mentioned that the most active metal (Al) in the intermetallic phase gets selectively dissolved leading to further enrichment of the phase with nobler metals like Fe and Mn causing an increase in the potential difference. The study also mentioned that both $Al(Fe,Mn,Cr,Si)$ and $Al_6(Fe,Mn)$ have a similar mechanism in formation of pits.

The electrochemical potential of Mg_2Si particle is more negative compared to the alloy matrix which denotes that the intermetallic phase have an anodic character. Even though the difference in potential is as prominent in anodic side as for $Al(Si,Fe,Mn,Cr)$ in cathodic side (see figure 2.8), the activity of Mg_2Si is comparatively lower than the Fe-rich intermetallic phases due to the passivation of Mg_Si intermetallic phases by the formation of hydroxides. Due to its anodic character, selective dissolution of Mg from the intermetallic was observed leading to an enrichment in Si content in the intermetallic. Due to the Si enrichment, the intermetallic phase transits to a cathodic character after the immersion into NaCl solution [31, 46].

The figure 2.10 shows Atomic Force Microscopy (AFM) images of in-situ experiments carried out in immersion test in 0.005 M NaCl solution. From the figure 2.5, one can note the crater like formation ofMg_2Si phase (markings #4 and #5) which was explained to be due to selective dissolution of Mg from Mg_2Si particle leaving behind a shallow hole. The depth of the crater have been reported to be in the range of few hundred nano-

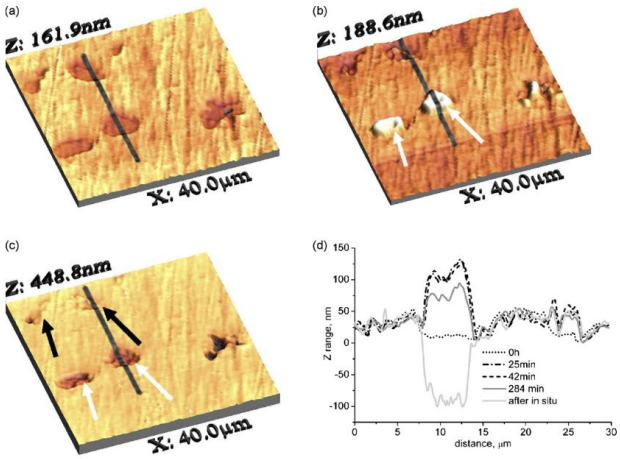

Figure 2.10: AFM images of AA5083 alloy in (a) as-polished (b)in-situ measurment after 25 minutes immersion, (c) after removal from in-situ electrolyte and cleaning condition and (d) the line profile at different immersion times. (Adapted from [31])

meters and not grow beyond that as shown in figures 2.10(c) and (d) . This restriction to dissolution of Mg_2Si particle beyond certain depth is explained by the formation of hydroxide layer on top of the intermetallic phases as shown as a white coloured hill in the figure 2.10(b). [31]

2.4.2. LOCALISED CORROSION IN AA6082

Chen et. al. [41] investigated the influence of Fe-rich intermetallic phases on the corrosion of Al-Mg-Si weld joints. It was found that the morphology and the size of the intermetallic phases has a significant impact on the pitting of the alloy matrix. Figure 2.11 shows the pitting damage caused by α (spherical) and β (needle-like) after immersion test in 3.5 wt% NaCl solution for 24 hrs. It can be observed that the needle-like β phase cause more severe pitting compared with the spherical α phase. $AlFeSi$ intermetallic phase exhibits more cathodic potential when compared with the alloy matrix which leads to anodic dissolution of metal matrix forming pits along the intermetallic and matrix interface. Further, most intermetallic particles that participated in pitting was observed to be be detached from the alloy matrix. However, the author has not mentioned about the corrosion progression after the intermetallic phase gets detached from the matrix.

The pitting was observed to be severe around β phase due to the increased area of contact when compared with the α phase. Due to the increase in contact area, higher dissolution of alloy matrix is promoted. Figure 2.12 represents a schematic of the intensity of pitting around α and β phase. Further, the β phase was observed to have Fe:Si ratio near to 1:1 whereas α phase was observed to have Fe:Si ratio of 2:1. The author have not mentioned anything explicitly about the relevance between the Fe:Si ratio and

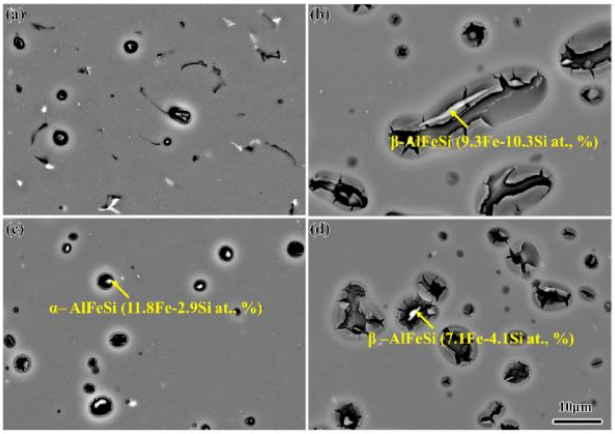

Figure 2.11: Pitting corrosion occurred in four different regions of the weld zones (Adapted from [33])

pitting susceptibility of the alloy.

But, knowing that the Si and Fe exhibits nobler potential than the alloy matrix and Si being further nobler than Fe, the higher amount of Fe present in α phase (2:1 Fe:Si ratio) narrows down the potential difference with respect to the alloy matrix leading to have lower pitting corrosion effect on the alloy matrix. Whereas with higher Si content the potential difference is enlarged leading to severe corrosion as like in β phase.

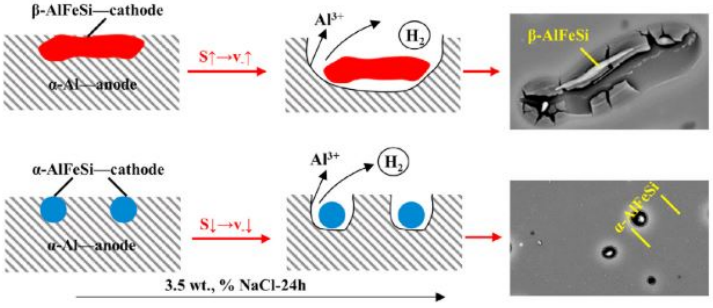

Figure 2.12: Schematic representation of pitting corrosion in α and β phases (Adapted from [33])

ZENG Feng-li et. al. [46] studied the mechanism of corrosion of Mg_2Si and Si phase in Al-Mg-Si alloy. The author differentiates two kinds of alloys with respect to $Mg-Si$ IMP formation and susceptibility to intergranular corrosion based on ratio of Mg and Si content in the alloy. When the Mg:Si content ratio is greater than 1.73, all the silicon combines and precipitates as Mg_2Si phase in the grain boundaries whereas when the Mg:Si ratio is less than 1.73, the excess silicon content precipitates as pure silicon particle in addition to Mg_Si phase along the grain boundaries.

The corrosion mechanisms of these two cases are completely different where intergranular corrosion is more prominent in the alloys with Mg:Si content less than 1.73 compared with the other. As explained previously the Mg_2Si phase initially acts as anodic inclusion and when the alloy comes in contact with corrosive environment, selective leaching of Mg from Mg_2Si phase occurs leaving behind a nobler phase rich in silicon. This silicon enrichment leads to a transformation from anodic to cathodic character of Mg_2Si phase. Since silicon is much nobler than the alloy matrix, the corrosion activity of pure silicon along the grain boundary follows anodic dissolution of the alloy matrix forming pits.

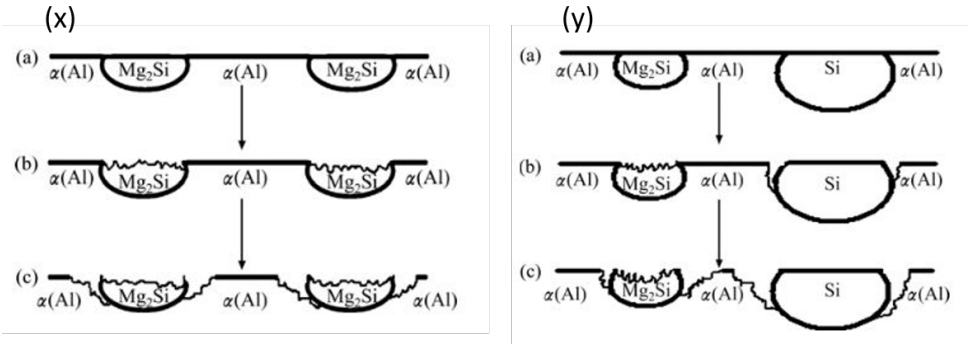

Figure 2.13: Schematic representation of corrosion when (x) only Mg_2Si particle is present and (y) both pure-Si and Mg_2Si are present (Adapted from [46])

Mg_2Si phase exhibits a discontinuous array of precipitation along the grain boundaries with areas of precipitate free zones (PFZs) in between the precipitates. The dissolution of aluminium from this PFZs determines whether the alloy is susceptible to IGC or not. When both pure-Si and Mg_2Si phases are present, the synergy of cathodic characters of both the intermetallic phases comes into play promoting IGC along the grain boundaries via dissolving aluminium from PFZs. Whereas in the presence of only Mg_2Si particles, there is no synergy but a general corrosion along and near the intermetallic phase. Figure 2.13(x) and 2.13(y) represents a schematic illustration of alloy having Mg:Si ratio more than 1.73 showing no IGC and alloy having Mg:Si ratio less than 1.73 showing susceptibility to IGC due to PFZ dissolution respectively.

2.5. CONCLUSION AND RESEARCH OBJECTIVES

Following conclusions can be made based on the literature survey -

- Localised corrosion is initiated due to the difference in electrochemical properties between the IMPs and the alloy matrix
- If the IMP is cathodic with respect to the alloy matrix trenching around the IMP due to material dissolution of the base alloy will occur

- If the IMP is anodic, selective dissolution of the most anodic phase inside the IMP will occur
- AA5083 and AA6082 has almost the same elements present in it but Si content is excess in AA6082
- Both AA5083 and AA6082 has two major group of IMPs - Fe-rich IMPs and $Mg-Si$ IMP.
- AA5083 - common IMPs are Al_6MnFe, $Al-(Si,Mn,Fe,Cr)$, Mg_2Si and βAl_3Mg_2. The formation of β phase happens after sensitization treatment of the alloy.
- AA6082 - common IMPs are $Al(Fe,Mn,Si)$ and Mg_2Si. Pure Si particles precipitate in alloys having Mg:Si content less than 1.73 $wt\%$.
- The Fe-rich phases act cathodic whereas $Mg-Si$ phase acts anodic with respect to the alloy matrix.
- Fe-rich phases are mostly cathodic with respect to the alloy matrix. The localised corrosion activity of these phases are such that it dissolves the Al around the phase forming a trench. The formed trench might get inactive due to particle fall-out from the trenched area where there is no drive for further localised corrosion.
- $Mg-Si$ phase can vary from being anodic to cathodic due to selective dissolution of Mg leading to enhancement of Si content. The $Mg-Si$ phase can become less active along the time due to formation of Mg oxides covering the IMP.

Following Research objectives are made considering the project motivation and the literature survey to better understand the localised corrosion activity due to the intermetallic phases present in AA5083 and AA6082 alloys -

- To understand the macroscopic corrosion behaviour of AA5083 and AA6082 alloys in different conditions which include UPW, Artificial Cooling Mixture/Water (ACW) and in Cl^- environment.
- To understand the electrochemical behaviour of IMPs present in these alloys and to correlate the effect of composition of the IMPs with its electrochemical behaviour
- To utilize localised techniques for corrosion and electrochemical behaviour monitoring of IMPs and to understand the general surface activity of both AA5083 and AA6082 alloy.
- To understand how the localised corrosion attach develops and the role of alloy composition and IMPs in pit initiation and propagation.

3

MATERIALS AND METHODOLOGY

3.1. MATERIALS

AA5083-O alloy and **AA6082-T6** alloy having cylindrical shape of thickness of 5 mm and circular diameter of 12 mm are utilised. Samples of both the alloys are provided by ASML. The table 3.1 and 3.2 shows the result of X-Ray Fluorescent Spectroscopy (XRF) elemental composition measurements carried out in Panalytical Axios Max WD-XRF spectrometer.

Table 3.1: Elemental composition of AA5083 Alloy in wt% obtained by XRF measurements.

Al Alloy	Al	Mg	Mn	Si	Cr	Fe	Ti	Zn	Cu
5083	93.43	5.24	0.80	0.18	0.13	0.11	0.04	0.04	0.03

Table 3.2: Elemental composition of AA6082 Alloy in wt% obtained by XRF measurements.

Al Alloy	Al	Si	Mg	Mn	Fe	Zn	Cu
6082	97.25	1.06	0.80	0.50	0.22	0.14	0.04

Comparing both the alloys it can be observed that -

- In AA5083, as expected the major alloying content is Mg.
- In AA6082, the major alloying content is both Si and Mg.
- AA5083 has additional Cr and Ti content in it whereas these elements are absent or undetected by the XRF spectrometer for AA6082 alloy

3.2. COMPOSITION AND MICROSTRUCTURE EVALUATION

3.2.1. SAMPLE PREPARATION

All the experiments are conducted on a mirror polished surface of the samples. SiC papers of grid size from 320 to 2000 were used to grind the sample surface and then it is

polished using diamond slurry of size 3 μm and then with 1 μm to obtain the mirror-like polished surface.

For the tests that required mounting, the samples were attached with copper tape at the back end and then cold mounted to fit the sample in the electrochemical cell. The figure 3.1 shows a schematic of the sample mounted in a non-conductive resin having a copper tape attached for connection to the potentiostat. Cold mounting was preferred to avoid any effect of temperature change on the sample and non-conductive resin was used for mounting to avoid the influence of resin on the electrochemical data.

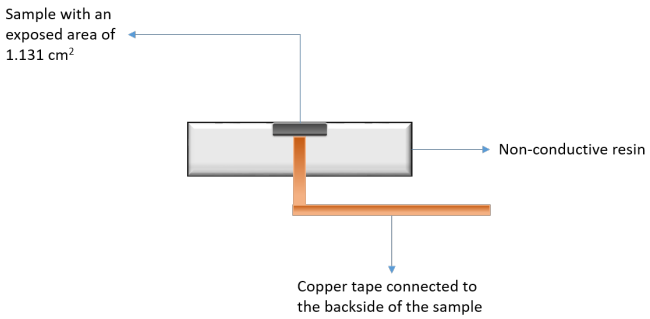

Figure 3.1: Picture of AFM-SKPFM setup showing different aspects.

3.2.2. SEM AND EDS

To view the intermetallic phases and the microstructure, Jeol JSM IT-100 scanning electron microscope (SEM) was used. The SEM is embedded with energy dispersive spectroscopy (EDS) which was used to determine the elemental composition of the alloy surface and the intermetallic phases.

3.3. MACRO-SCALE ELECTROCHEMICAL STUDIES

3.3.1. TEST SETUP AND CONDITIONS

The macroscopic electrochemical tests helps in studying the overall corrosion performance of the material in an accelerated test condition as the results obtained corresponds to a relatively large area of the sample. The electrochemical tests were carried out in 3-electrode cell setup with the help of Biologic VSP-300 potentiostat and the EC-Lab V11.43 software was used for data collection and analysis. The setup used for the experiments is shown in the figure 3.2.
The 3-electrode cell setup consist of -

- **Reference Electrode** - Ag/AgCl in saturated KCl solution
- **Counter electrode** - Stainless Steel mesh
- **Working electrode** - the test sample

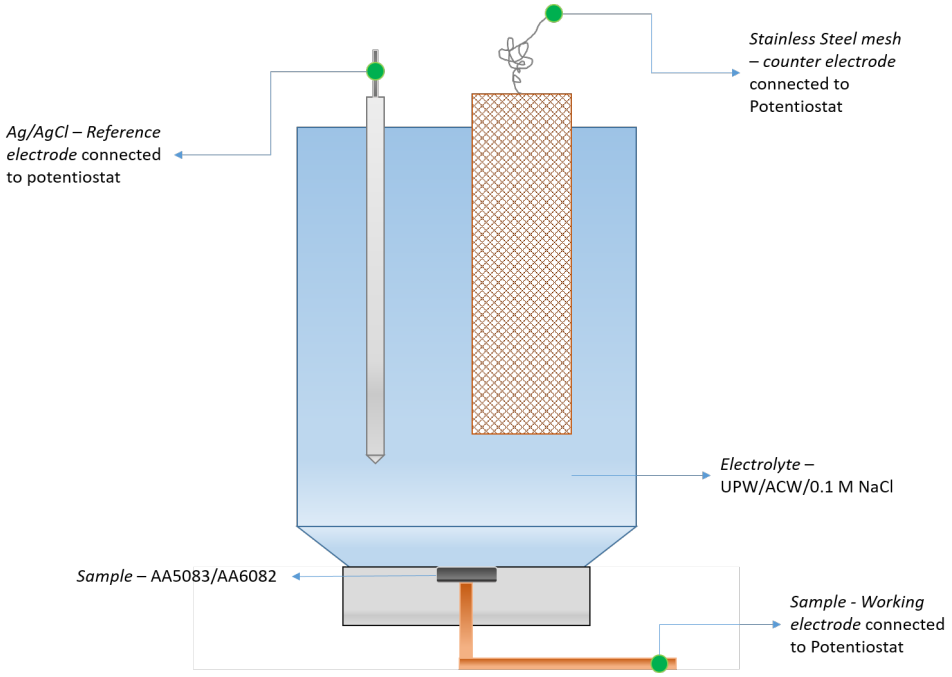

Figure 3.2: Schematic representation of 3-electrode cell setup used.

The samples were tested in three different conditions -

- Ultra Pure Water (UPW)
- Artificial Cooling Water (ACW)
- 0.1 M NaCl in UPW

Testing in UPW condition closely mimics the scenario in ASML cooling water circuits at initial stages where the inner walls of the cooling channels are exposed to UPW. The Artificial Cooling Water (ACW) as the name states, is artificially created by ASML by mixing different types of ions to closely relate to the state of UPW's condition after several years of contamination. The table 3.3 lists the ions that are added to the UPW to create the ACW recipe. Testing in ACW condition is necessary to understand the materials behaviour at some point in time where the UPW gets contaminated.

Since the UPW and ACW conditions are generally very low in ion concentration, corrosion monitoring through immersion testings will consume huge amount of time, exceeding the project timeline, to get to useful conclusions. Further, UPW and ACW conditions are of two extremes where the former has no ions and the latter has large variety of ions where each one of them will have a different mechanism of corrosion or inhibition depending on the type of ions.

Table 3.3: Ion composition and concentration added in UPW to create the ACW.

Ion Type	Concentration (mg/l)
Al	0.40
Si	1.48
Ca	0.19
K	0.05
Na	1.54
Mg	0.07
Cu	0.5
Ni	0.80
Cl^-	2.14
${NO_3}^-$	0.025
${PO_4}^{3-}$	0.11
P	0.02
${SO_4}^{2-}$	2.13
S	0.79

Considering these limitations, an additional testing condition in 0.1 M NaCl solution is included to specifically target and accelerate the localised corrosion testings in immersive conditions. 0.1 M concentration will help in accelerating the tests and since the solution has a single varient of ion i.e. the Cl^- ions, the variables are in control and hence conclusions can be made simpler.

In addition, the pH of the solutions were kept in close range and near to the neutral pH of 7 to eliminate the extra variable of the effect of pH on the corrosion behaviour of the two alloys.

3.3.2. TESTING SEQUENCE

The testing sequence of the macro-scale electrochemical tests followed the order -

Open Circuit Potential (OCP): The samples are first exposed to the electrolyte for 30 minutes and the open circuit potential is measured.

Potentiodynamic Polarisation (PDP): Until now the sample is under non-destructive measurement condition. After EIS measurements, the sample is subject to a destructive polarisation test where the sample is biased from a potential lower to the OCP to a potential higher the the OCP and the respective cathodic and anodic currents are measured. In this setup the potential is varied from $OCP - 0.250$ to $OCP + 1.0\ V$ with a scan rate of $+1\ mV/s$ for all the samples and conditions.

Microscopic Examination: After performing the corrosion experiment on the sample, the sample surface is examined and analysed using SEM-EDS technique.

3.4. LOCALISED CORROSION EVALUATION

3.4.1. SURFACE MORPHOLOGY AND VOLTA POTENTIAL MEASUREMENT

BACKGROUND

Scanning Kelvin Probe Force Microscopy (SKPFM) is a technique based on Atomic Force Microscopy (AFM) technique to determine the contact potential difference between the conductive cantilever tip and the sample surface. This contact potential difference is called the Volta potential or the volta potential difference. As the tip scans an area containing intermetallic phases, due to the change in composition of the intermetllic phase and the alloy, there will be a change in there work function too. This changes in the work function will be reflected in the volta potential measurement [47].

AFM-SKPFM is a very useful technique where the volta measured can be directly correlated with the electrochemical activity of the intermetallic phases and the alloy [48, 49]. Many studies have took advantage of AFM-SKPFM technique to understand the localised corrosion activity of the material studies [50–55].

Tapping Mode or intermitted contact mode in AFM has the tip positioned close to the surface and oscillated at the resonance frequency of the cantilever tip. In this mode, the tip taps the surface and depending on the electrostatic attraction or repulsion force imparted on the tip due to van der Wall's forces between the tip and sample, there will be a change in the frequency and amplitude of oscillation of the tip. Usually, the AFM is operated in Frequency Modulation (FM) mode where the feedback system analyses the changes in the frequency to have high resolution imaging compared with Amplitude Modulation (AM) mode [56, 57]. As depicted in figure 3.3, the feedback frequency and the amplitude signal in tapping mode are shown.

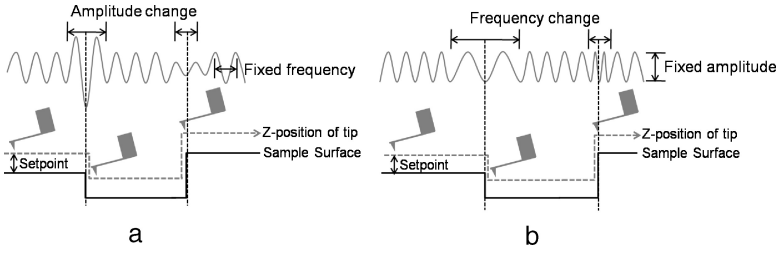

Figure 3.3: Schematic representation of (a) AM and (b) FM feedback modes in tapping mode of AFM tip. (Adapted from [57])

Volta Potential (VP) or Contact Potential Difference (CPD) given by V_{VP} between the sample and the tip is defined as in the equation 3.1 where Φ_{tip} and Φ_{Sample} are the work function of the tip and sample respectively and e is the electronic charge.

$$-eV_{VP} = \Phi_{tip} - \Phi_{Sample} \tag{3.1}$$

Figure 3.4 shows the schematic of changes in the fermi levels (E_{fs} and E_{ft}) of sample and tip when separated by a large distance (d) (figure 3.4(a)) and when the sample

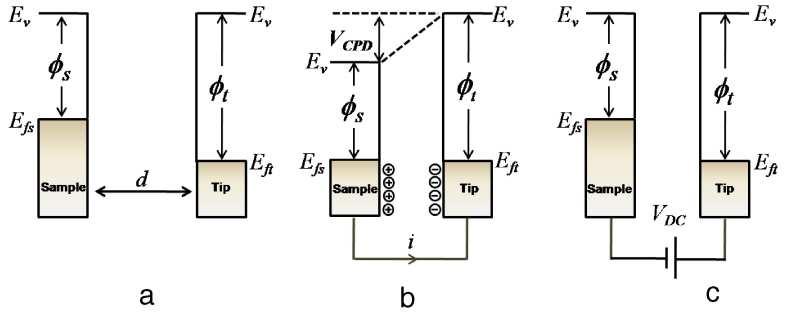

Figure 3.4: Schematic representation of changes in fermi energy when sample and tip are (a) far apart, (b) close to each other and (c) when an external bias equal to the difference in work function is applied. (Adapted from [57])

and tip are brought closer where current flow (i) is established due to flow of electrons from higher fermi energy state to the lower fermi energy state (figure 3.4(b)) equating the fermi levels of the sample and tip. At this stage surface charges comes to play to established CPD and in return the electrical force between the tip and the sample. An external Direct Current (DC) bias is applied either to the tip or sample where the amount of the DC bias that cancels out the electric force generated by the CPD equals to the CPD itself.

To calculate the CPD, an a combination of Alternating Current (AC) voltage (V_{Ac}) and DC voltage (V_{DC}) is supplied to the SKPFM tip where AC voltage generates establishes an oscillating electrical force. The total electrostatic force (F_e) generated is given by equation 3.2 where $\frac{dC_z}{dz}$ is the capacitance gradient between sample and tip, and ΔV is the total potential difference between sample and tip given by equation 3.3.

$$F_e = -\frac{1}{2}\frac{dC_z}{dz}\Delta V^2 \tag{3.2}$$

$$\Delta V_{tip} = V_{external} \pm V_{VP} = (V_{DC} \pm V_{VP}) + V_{AC}\,sin(\omega t) \tag{3.3}$$

By applying the external AC and DC bias, the tip is superimposed with electrical force oscillation in addition to the mechanical oscillation. A lock in amplifier is used to extract the electrical force component which can be obtained from solving the equations 3.2 and 3.3. This electrical force component is used to measure the CPD i.e. the volta potential. The changes in AFM-SKPFM tip position and hence the calculation of force components and volta potential is carried out with the help of laser which is incident on the AFM-SKPFM tip and reflected into a photo-diode in the feedback system shown in figure 3.5.

TESTING CONDITION AND SEQUENCE

Bruker Dimension Edge with Scan Asyst AFM equipment placed on a vibration isolated surface was used. The measurements were carried out in air and in a closed environment. Bias potential of 6 V was applied on the tip and two-pass scan technique was used; where the first pass measures the topology by the AFM tapping mode and the tip

is lifted 0.1μm for the second pass which measures the volta potential.

To evaluate the localised corrosion activity around the intermetallic phases based on the surface morphology and volta potential measurements the following steps are followed:

Step 1: Area of 100 μm × 100 μm are marked on the polished sample surface through indentation to identify the location of the intermetallic phases throughout the experimental sequence.

Step 2: Intermetallic phases inside the marked region are selected and AFM-SKPFM measurements were carried out on it.

Step 3: SEM images of the scanned intermetallic phases are captured and elemental composition of the same were also performed with the help of EDS.

Step 4: The sample is then immersed in 0.1 M NaCl solution for 4hrs duration and the steps 1 and 2 are repeated after immersion.

Step 5: Finally, the sample is again immersed in 0.1 M NaCl solution for additional 4 hrs and step 3 is followed.

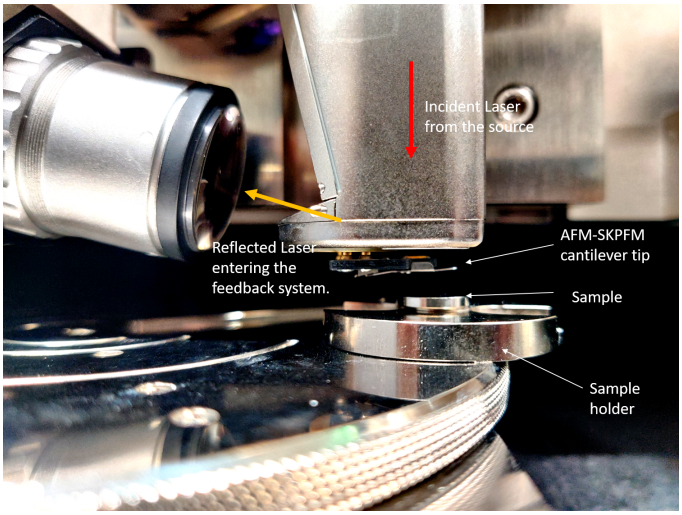

Figure 3.5: Picture of AFM-SKPFM setup showing different aspects.

3.4.2. IN-SITU SURFACE ACTIVITY MONITORING

BACKGROUND

Scanning Electro-Chemical Microscopy (SECM) is a technique utilised to image the redox activity happening on the metal surface using an Ultra Micro Eleectrode (UME) - SECM probe as the working electrode and a redox mediator [58–60]. Several studies have used this technique for in-situ monitoring of localised corrosion and pitting behaviour [59–67].

The UME is a platinum (Pt) wire enclosed in a glass casing which detect the activity on the surface of the metal. In SECM measurements when sample is unbiased, the activity on the surface is monitored with the help of three electrode system where the UME acts as working electrode, Ag/AgCl as reference electrode and a platinum strip as counter electrode. The sample is immersed in the electrolyte which is mixed with typically a milli molar concentration of the redox mediator. Figure 3.6(x) shows a schematic of SECM setup with the sample also being connected to the potentiostat. The sample is fixed in a position and the probe is moved over the surface with the help of position controller to scan the required area.

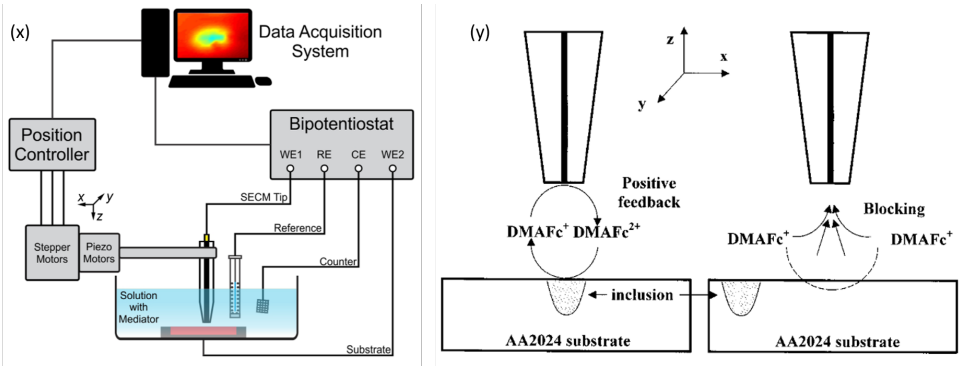

Figure 3.6: (a) Schematic representation of the setup used for in-situ SECM monitoring when sample is also connected to potentiostat (adapted from [68]). (b) Schematic representation of imaging mechanism for the mediator (dimethylamino methylferrocene - DMAFc) when showing positive feedback (left) and blocking effect (right) (adapted from [59]).

Figure 3.7(b) shows the CV curve measured for FcMeOH mediator in 0.1 M NaCl solution when the tip is held far away from the surface. At a large distance of separation of tip and sample, for a mediator with N number of electrons involving in redox reaction, bulk concentration C and diffusion coefficient D, the steady state current (I_{ss}) is given by equation 3.4 where F is the Faraday's constant and a is the Pt tip radius. The probe is biased at a potential to have the oxidation of the mediator controlled by diffusion.

$$I_{ss} = 4NFDCa \tag{3.4}$$

The feedback current signal is affected by distance of separation between the sample and probe, and whether the probe is above a conductive/active region or non-conductive/inactive region. The probe is always positioned at a constant distance of separation with

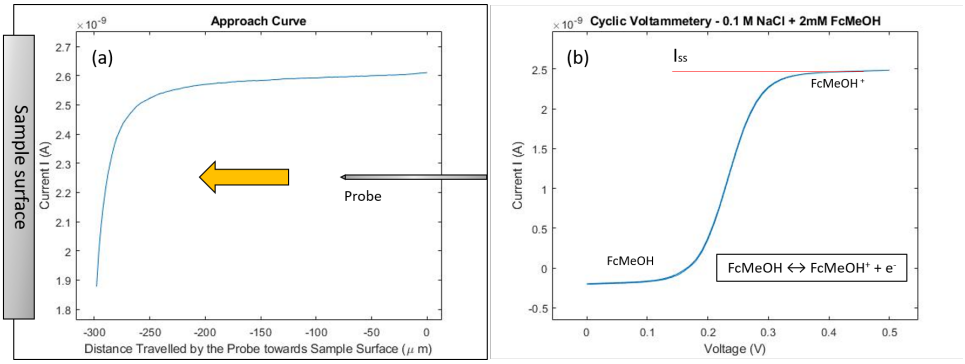

Figure 3.7: (a) Approach curve and a schematic representation of probe approaching the sample surface. (b) Cyclic voltammetery (CV) curve showing the redox reaction involved and the output steady state current (I_{ss}).

respect to the sample when performing experiments to eliminate the effect of distance on the output signal.

At a short and constant distance of separation, when the scanning spot on the sample surface is conductive/active, which usually corresponds to the intermetallic phases in this case, the oxidised mediator at the tip gets readily reduced by the active spots due to its cathodic nature. This rapid cyclic oxidisation and reduction happening on top of active spots of the sample increases the overall current output in the system (refer to figure 3.6(y)). The current output will be typically higher than the I_{ss} resulting in positive feedback at active spots.

At inactive/insulated spots, which usually corresponds to the alloy matrix away from the intermetallic phases, at the same distance of separation, the current output is lower than the I_{ss} due to blocking effect (refer to figure 3.6(y)). The blocking effect occurs due to the lowered concentration of mediator between the separated distance and also due to the hindered diffusion at this close range. This effect can also be seen in the approach curve (figure 3.7(a)) where the current output is suddenly drops when the probe approaches closer to the non-conductive surface. In this case, the non-conductive surface is the mold resin where the sample is mounted.

TESTING SEQUENCE

The SECM tests performed using Uniscan Instruments PG580R potentiostat and SCV370 control unit having the following elements in operation -

1. **Reference Electrode:** Ag/AgCl
2. **Counter Electrode:** Pt strip
3. **Working Electrode:** UME of Pt wire diameter of 10μm (see picture 3.8)
4. **Redox Mediator:** Ferrocenemethanol (FcMeOH)

5. **Electrolyte:** 0.1 M NaCl solution mixed with 2 mM FcMeOH

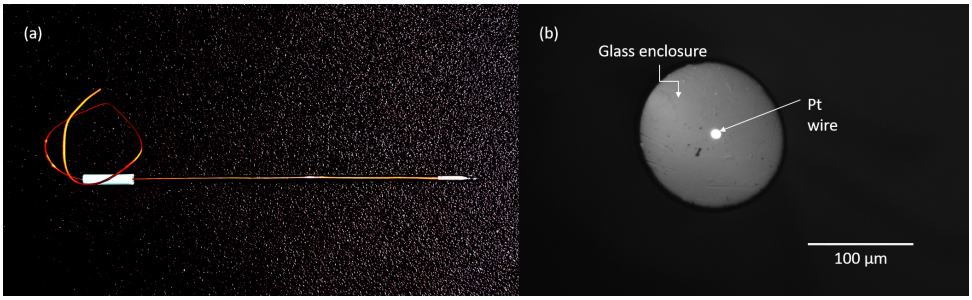

Figure 3.8: (a) Picture of SECM probe and (b) optical microscopy image of SECM tip showing Pt wire enclosed inside glass rod

The procedures that are followed to setup the experiment are as follows -

Step 1: **Probe Cleaning** is first carried out to ensure the probe is clean before every experiment. The cleaning is carried out in 0.5 M H_2SO_4 solution where the probe is applied with a a voltage sweep from -1 V to 1 V for 10 cycles.

Step 2: **The Sample** is mounted and mirror polished for SECM measurements. The sample surface is covered by a tape and the outer walls of the sample mold is attached with a strong tape around it and protruded on one side to hold the electrolyte without any leakage (see the green tape in figure 3.9). The sample is then fixed on the stage and rough leveling through bubble level is carried out.

Step 3: **3 Point Leveling through Probe Approach** is carried out where the probe is slowly lowered closer to the covering tape attached on top of the surface at 3 locations in triangular fashion having 1 mm lateral distance with respect to each location. The approach curve (see figure 3.7(a)) is current (I) vs distance curve where the sudden drop in output current denotes that the blocking effect is way too high and hence the probe almost touches the sample's surface at that approach distance. The sample is levelled until the approach distance is equal in all the three locations. Precise levelling is carried out to eliminate the effect of sample tilt on the output SECM maps and also to avoid the probe touching the sample surface when scanning.

Step 4: **Probe Approach on Mold** is carried out by removing the covering tap on the sample surface where the same approach curve is used to position the probe tip at a constant distance of separation from the sample surface. Since the approach curve works with the blocking effect, the approach is carried out on the mold as it is non-conductive hence, avoiding any active spots from the sample surface.

Step 5: Finally, the the probe is positioned on top of the sample surface and the scanning is initiated after providing the necessary parameters to the software.

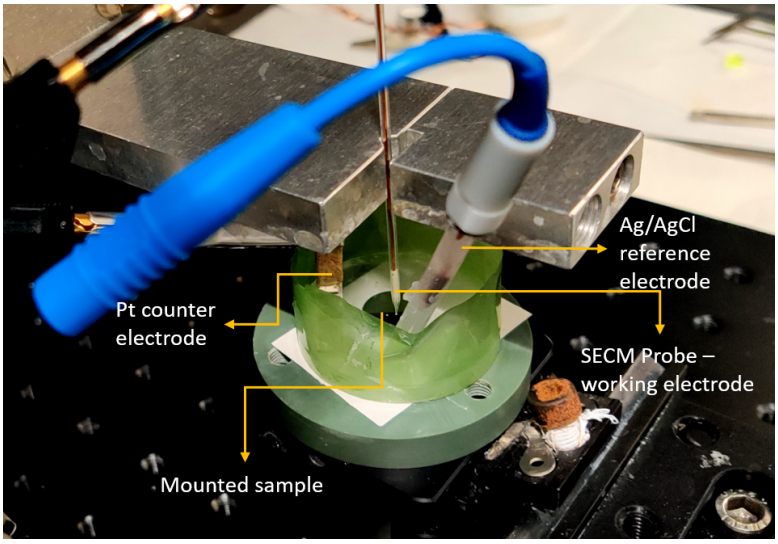

Figure 3.9: Picture of the setup used for in-situ SECM monitoring of the sample surface activity.

There are two different kinds of scanning are carried out to extract useful data for the materials and they are -

1. **FcMeOH Scan:** In this scan, the probe is biased at a potential of 0.5 V (vs Ag/AgCl) where the oxidisation of the mediator (FcMeOH) happens at the probe tip and the output signal depends on how fast the redox reaction ($FcMeOH \leftrightarrow FcMeOH^{+} + e^{-}$) is happening depending on whether the probe approaches on a active spot or inactive spot.

2. **Oxygen Scan:** The purpose of this scan is to map differentiate between cathodic and anodic intermetllic phases by its variation in consumption of oxygen. It is well know that on top of cathodic intermetallic phases, oxygen and water is reduced as a counter cathodic reaction for anodic dissolution of Al around the phase where the same mechanism is not followed for anodic intermetallic phases. Here, the SECM probe is used in redox competition mode where the probe is biased at -0.7 V (vs Ag/AgCl) to initiate the diffusion controlled oxygen reduction reaction at the probe tip [69, 70]. The probe detects a constant current output unless it is on top of a cathodic particle where the output current is lowered due to decrease in available oxygen content between the tip and cathodic particle. The decrease in output current in specific regions denotes the presence of cathodic intermetallic particles [71].

4

RESULTS AND DISCUSSION

4.1. MICROSTRUCTURE AND INTERMETALLIC PHASES

The SEM images of polished AA5083 and AA6082 alloys (see figure 4.1) shows the presence of two major kind of intermetallic phases having brighter and darker shades. The phases showing bright shade corresponds to Fe-rich intermetallic phases whereas the darker ones corresponds to Mg-Si based intermetallic phases.

In AA5083 alloy the Fe-rich intermetallic phases are of type $Al(Fe, Si, Mn, Cr)$ and Mg-Si based phases follows the stochiometery of Mg_2Si whereas in AA6082 alloy, the Fe-rich phases are of type $Al(Fe, Mn, Si)$ and the Mg-Si phases follows the similar stochiometery of Mg_2Si as in AA5083. Figure 4.2 shows the EDX spectrum of Fe-rich and Mg-Si intermetallic phases of AA5083 and AA6082 alloys respectively.

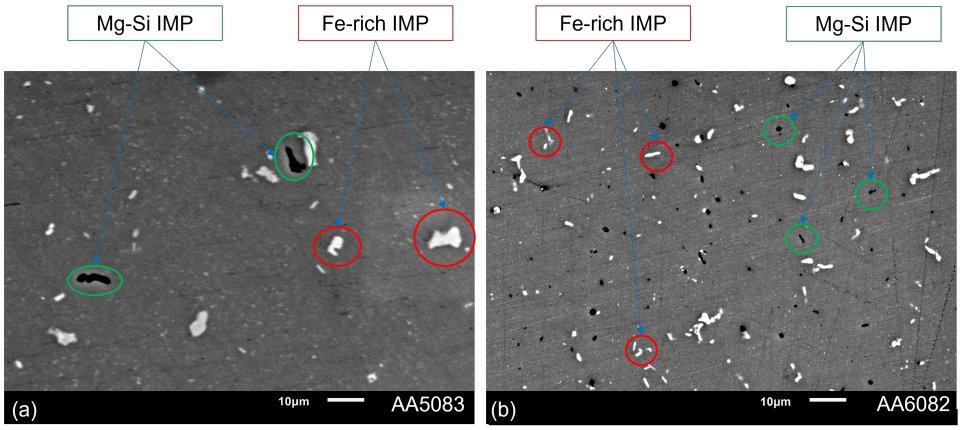

Figure 4.1: SEM micrographs showing Fe-rich IMPs and Mg-Si IMPs of (a) AA5083 and (b) AA6082 alloys.

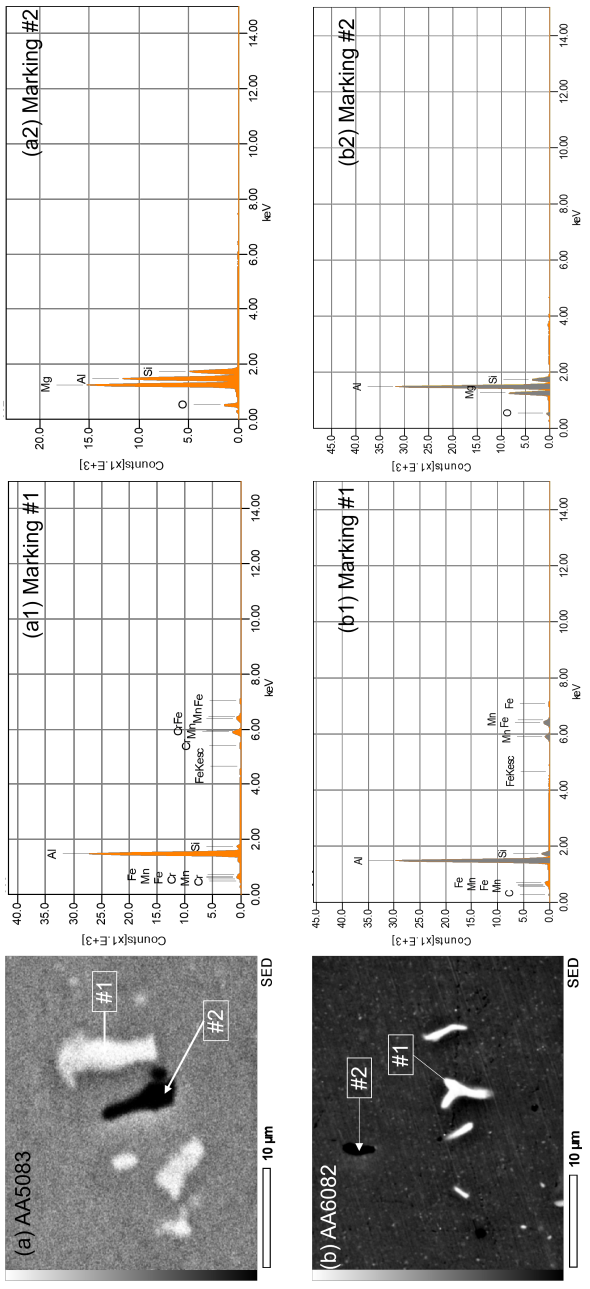

Figure 4.2: Single point EDX spectrum of marked spot on the SEM image of polished (a) AA5083 and (b) AA6082 sample. Marking #1 corresponds to Fe-rich intermetallic phase and marking #2 corresponds to Mg-Si phase.

4.2. MACRO-SCALE ELECTROCHEMICAL BEHAVIOUR

4.2.1. OPEN CIRCUIT POTENTIAL (OCP)

For both AA5083 and AA6082 alloys in UPW condition, the OCP values (refer to figure 4.3) can be observed to be very quite stable whereas in ACW and NaCl conditions, the OCP values exhibit a noisy behaviour. These noises can be a result of an increased activity on the metal surface due to the presence of corrosive ions in the electrolyte when compared with the case of UPW.

Further, it can be observed that both the alloys in ACW condition shows nobler potential compared with UPW and NaCl condition. This behaviour can be a result of the presence of phosphate ($PO_4{}^{3-}$), sulphate ($SO_4{}^{2-}$) and nitrate ($NO_3{}^{-}$) ions (refer to table 3.3) which are known to exhibit an inhibiting nature in neutral solution for aluminium alloys [72–74].

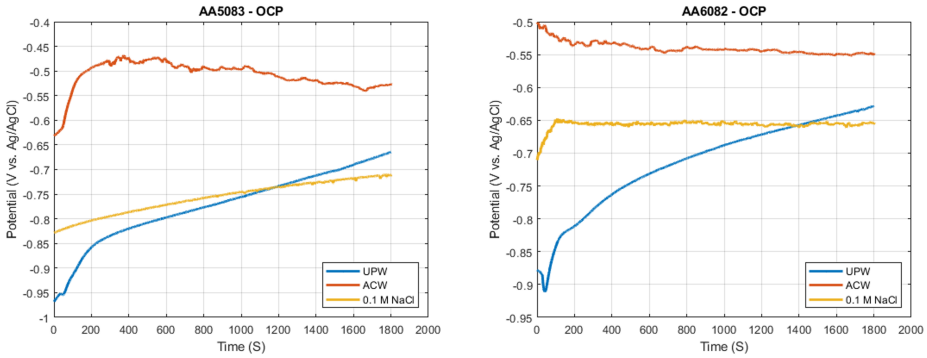

Figure 4.3: Open circuit potential (OCP) monitored for 30 minutes for AA5083 (left) and AA6082 (right) alloys in different conditions.

4.2.2. POTENTIODYNAMIC POLARISATION (PDP)

Figure 4.4 shows the potentiodynamic polarisation curves for AA5083 and AA6082 alloys in various conditions. Similar trends can be observed in the variation of corrosion potential (E_{corr}) across different conditions for both the alloys whereas the trend for corrosion current (I_{corr}) is different for these alloys (refer to figure 4.5). AA5083 shows a very similar I_{corr} value in all the conditions whereas AA6082 shows an increase in I_{corr} value where the lowest is observed in UPW followed by ACW and then 0.1 M NaCl environment.

The corrosion rate (r) for a pure metal is determined by the equation 4.1 where, a is the atomic weight of the metal, n is the number of electrons participating in the reaction, F is the Faraday's constant, D is the density of the metal and i is the current density. To determine the corrosion rate I_{corr} is used in the equation.

$$r = \frac{ai}{nFD} \tag{4.1}$$

Since the corrosion rate is directly proportional to I_{corr} and every other variables in equation 4.1 is almost the same for AA5083 and AA6082 alloys, the corrosion rate follows the same trend as I_{corr}.

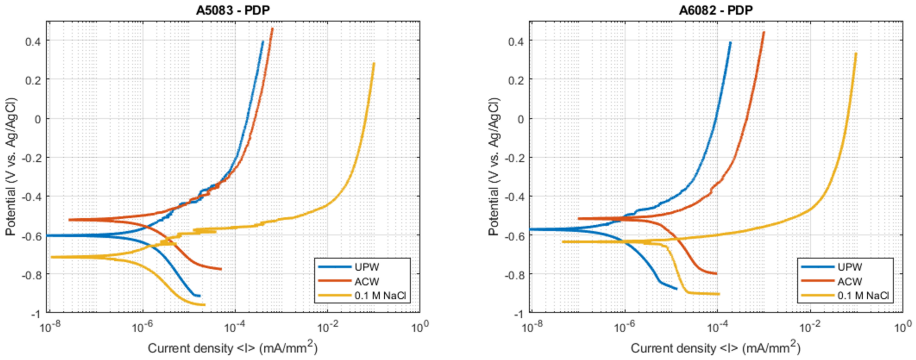

Figure 4.4: Potentiodynamic polarisation curves for AA5083 (left) and AA6082 (right) alloys in different conditions.

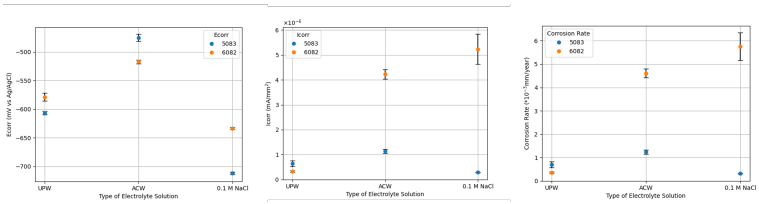

Figure 4.5: Potentiodynamic polarisation curves for AA5083 (left) and AA6082 (right) alloys in different conditions.

For AA5083 alloy, from figure 4.5 it can be observed that the corrosion rate is minimum for 0.1 M NaCl solution when compared with other two conditions. This is not something to be expected as the increase in corrosive Cl^- ions in the environment should increase the corrosion in general. However, it should be understood that the method (equation 4.1) used to determine the corrosion rate is only limited to estimating uniform corrosion type but it is know that the corrosion mechanism followed generally by aluminium alloys are by localised corrosion and pitting. Hence, this corrosion rate estimation through I_{corr} value do not cover the entire picture. This is very evident from the polarisation curves from figure 4.4 where even though the I_{corr} for AA5083 is similar in all the environments, the alloy encounters comparatively very large increase in current in the anodic region at potential above the respective E_{corr} value only in 0.1 M NaCl environment denoting that the alloy undergoes severe pitting. The severe pitting can also be observed for AA6082 alloy (see figure 4.4).

Further, from the polarisation curves (figure 4.4) it is interesting to note two other features; firstly, the clear occurance of metastable pitting in AA5083 in all the environments compared with AA6082 alloy and secondly, the negligible resistance to pitting

(difference between pitting potential E_{pit} and E_{corr}) observed in 0.1 M NaCl environment for AA6082 alloy. The reason behind this occurrence will be discussed later in this chapter.

4.2.3. MICROSTRUCTURE ANALYSIS AFTER POLARISATION

AA5083 - UPW

Figure 4.6 (a) shows the SEM image of AA5083 sample after polarisation in UPW. The markings #1 and #2 shows dark contrast around the edges of the bright Fe-rich IMPs denoting the trench formation. The trench is formed due to the cathodic nature of the Fe-rich IMPs which lead to dissolution of Al matrix around the IMP. These trenching behaviour were found in most of the Fe-rich IMPs all over the surface.

The marking #3 reveals pit formation in branched manner and looking closer in it, the IMPs which was initially responsible for the pit formation can also be found in the branches. It can be understood here that the formation of larger pits starts by occurrence of small trenching around the IMPs. As the trenches formed around the IMPs in close range grows, they get connected to each other leading to a larger spread of material dissolution in branched fashion. These large pit formation is found rarely on the surface in UPW condition as there is no corrosive ions to increase the chance of pitting and propagating it deeper into the material.

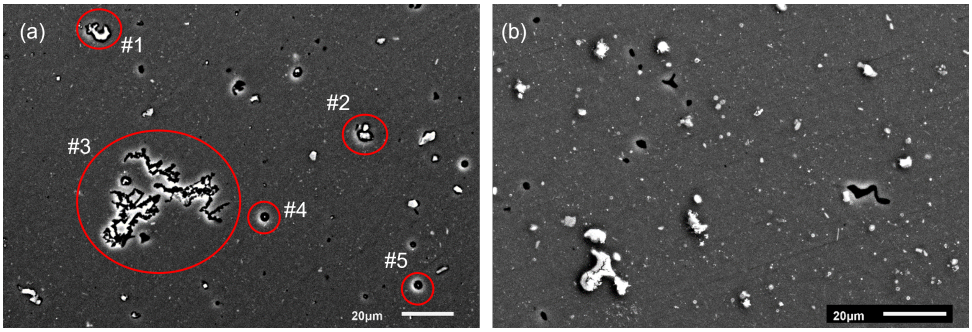

Figure 4.6: SEM images of AA5083 samples after polarisation in (a) UPW and (b) ACW environment.

Further, it is interesting to note the markings #4 and #5 where a small bright spot is visible at the middle of the trenched region. This bright spots are found to be titanium (Ti) particles revealed through EDX spectroscopy. These Ti particles behave cathodic with respect to the Al matrix and are found having a short needle like shape of length less than $1\mu m$. These particles were undetectable due to its size and/or indistinguishable from Fe-rich intermetallic phases due to its bright appearance in as-polished surface. They were easy to detect only after corrosion due to the circular trench around them.

AA5083 - ACW

Figure 4.6 (b) shows the SEM image of AA5083 sample after polarisation in ACW. The Fe-rich intermetallic phases after polarisation in ACW were found to reveal a patch like

deposition on top of it. These patches are detected to contain a mixture of Cu and S deposits but a clear definition was unable to be understood from EDX spectroscopy. These kind of depositions could originate from the environment (ACW in this case) containing the substance, as reported elsewhere [75–77].

AA5083 - 0.1 M NaCl

Figure 4.7 shows two different magnification of AA5083 surface after polarising in 0.1 M NaCl solution. Due to the presence of comparatively larger amount of highly corrosive Cl^- ions, as expected, the amount of pitting occurred on the surface was found to be very high and the same is evident from the figure 4.7 (a).

Similar to the case of AA5083 surface exposed to UPW, figure 4.7 (b) shows trenching around the intermetallic phases. Here, the marking #1 shows the trench happened around Ti particle and marking #2 shows trenching around the Fe-rich intermetallic phase. Further by looking the pit in figure 4.7(b), it can be observed that the trenching around the Fe-rich IMP (marking #3) has contributed in the development of pitting in that region. From this it can be understood here that, the trench around the IMPs acts as a reservoir for the Cl^- contained solution where the Cl^- ions can further fuel the pitting process leading to deeper propagation of pits.

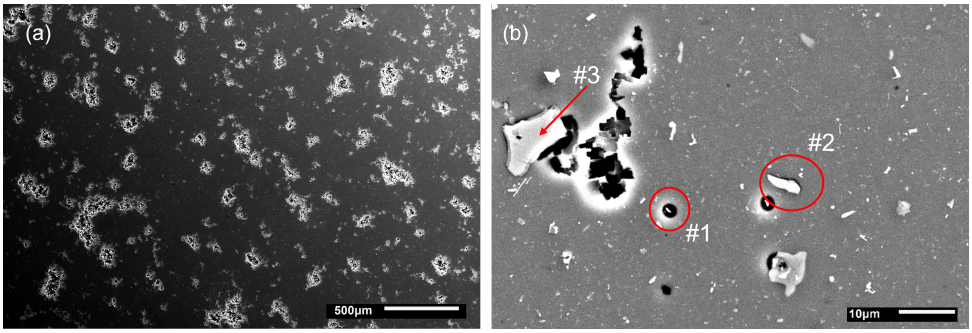

Figure 4.7: (a) Lower and (b) higher magnification SEM images of AA5083 samples after polarisation in 0.1 M NaCl solution.

AA6082 - UPW

Trenching around the Fe-rich intermetallic phases and rare pitting similar to the case of AA5083 alloy was observed in AA6082. Figure 4.8 (a) shows the SEM image of AA6082 sample surface after polarising in UPW environment. Similar pitting mechanism as AA5083 can also be observed in AA6082 where the presence of Fe-rich intermetallic phase can be found in the pit.

AA6082 - ACW

Figure 4.8 (b) shows the SEM image of AA6082 sample after polarisation in ACW environment. Similar Cu deposits on top of Fe-rich intermetallic phases can be observed as in the case of AA5083 samples. Interestingly, unlike A5083 a dome of oxide deposites can also be found on the pit.

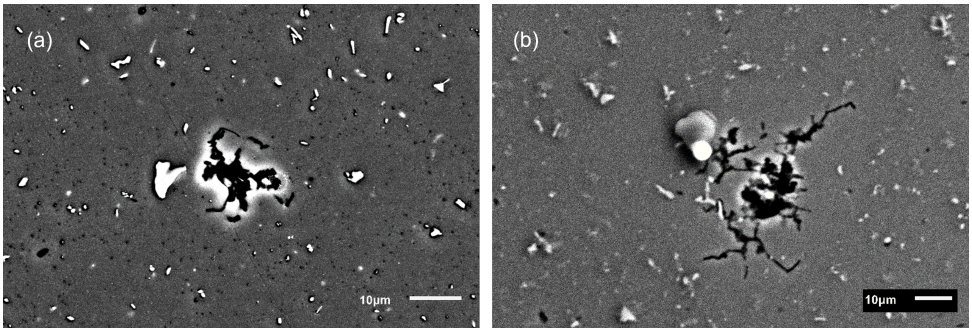

Figure 4.8: SEM images of AA6082 samples after polarisation in (a) UPW and (b) ACW environment.

AA6082 - 0.1 M NaCl

Figure 4.9 shows the SEM images of AA6082 sample surface subjected to potentiodynamic polarisation in 0.1 M NaCl solution. The amount of pitting occurrence on the surface is very similar to the case of AA5083 but the pit opening on the surface shows a dome like accumulation of oxides. They are characterised EDX spectroscopy to be oxides of aluminium which would have accumulated outside the pit due aluminium dissolution from deep inside the pit.

Figure 4.9 (b) also reveals the trenching happening around the intermetallic phases leading to pit initiation and propagation.

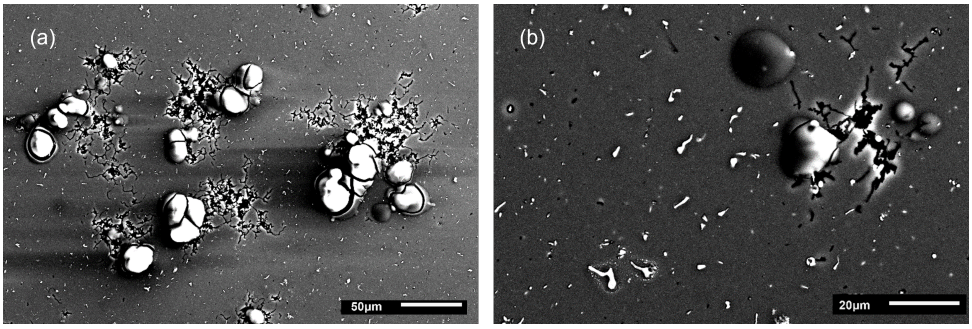

Figure 4.9: (a) Lower and (b) higher magnification SEM images of AA6082 samples after polarisation in 0.1 M NaCl solution.

In all these cases, based on the SEM images, no inferences can be obtained for $Mg-Si$ intermetallic phases due to its dark contrast.

4.3. ELECTROCHEMICAL ACTIVITY OF INTERMETALLIC PHASES

As discussed earlier in chapter 3, to study the electrochemical activity of intermetallic phases, immersion studies were carried out. The changes in topology and vota potential of a selected region containing the specific intermetallic phase before and after immersion for 4 hrs in 0.1 M NaCl solution were analysed with the support of respective SEM images.

4.3.1. INTERMETALLIC PHASES OF AA5083

FE-RICH INTERMETALLIC PHASES

Fe-rich intermetallic phases of AA5083 are known to exhibit cathodic behaviour and from the AFM-SKPFM Volta potential map shown in figure 4.10 (a2) and (b2) the same can be observed from the lowered of Volta potential with respect to the Al matrix at the intermetallic phase. Further, from the Volta potential profiles in figure 4.10 (c), the following observations can be made;

1. Slight reduction of cathodic peak after immersion
2. Increase in cathodic character of the surrounding Al matrix after immersion and hence a slight broadening of the peak

K.A. Yasakau et al. [31] reported that the effect of increase in cathodic character of the Al matrix decreases as the distance from the inermetallic phase increases. This effect is attributed to the anodic polarisation of the near-by surrounding Al matrix by the cathodic intermetallic phase due to the cathodic process. This anodic polarisation lead to an increase in native-oxide film thickness and consequently a change in Volta potential.

From the analysis of topology maps before and after immersion (refer to figure 4.10 (a1) and (b1) respectively), no note-worthy changes are observed except in figure 4.10 (b1) (reflected also in (b2)) where contamination like particles can be seen floating. By close observation, these seemingly floating particles has the same shape and orientation everywhere denoting artifact from the AFM-SKPFM tip.

No significant changes in topology (refer to topology in figure 4.10 (c)) reveals that within the immersion time of 4 hrs in 0.1 M NaCl solution no trenching behaviour is observed around the intermetallic phase. This in turn suggests that the intermetallic phase is getting less active over the time of immersion. The slight reduction and broadening of cathodic peak after immersion also suggests the reduction in activity of the Fe-rich intermetallic phase.

This reduction of activity can also arise from the presence of chromium (Cr) in the alloy which forms protective oxides. It is well established from the studies of steels that oxides of chromium are very stable and are protective against corrosion. Further, from EDX spectroscopy measurements (refer to figure 4.22 later in this chapter), it is interesting to note that the Cr is not localised to Fe-rich intermetallic phase but are uniformly distributed all over the alloy irrespective of intermetallic phases or the Al matrix. If in the case of localised presence of Cr, the cathodic character of Cr with respect to Al may

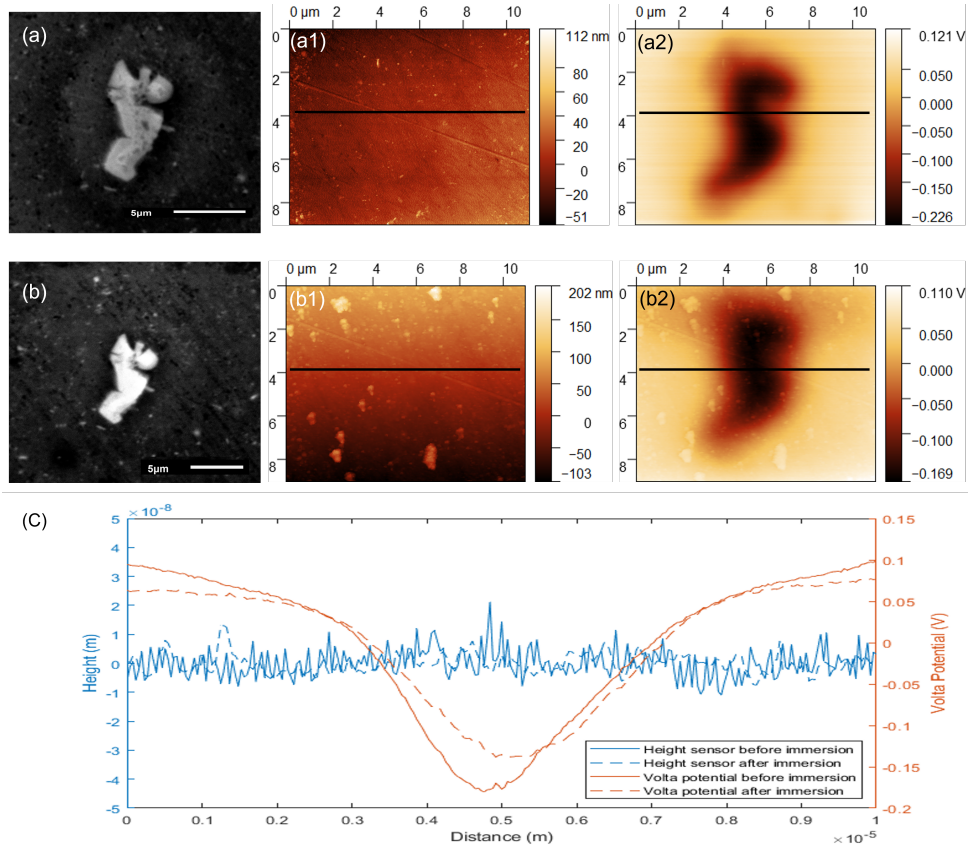

Figure 4.10: (a), (a1) and (a2) are the SEM image, topology map and the Volta potential map of Fe-rich intermetallic phase of AA5083 sample before immersion and (b), (b1) and (b2) are the counterparts after immersion in 0.1 M NaCl solution for 4 hrs. (c) Plot showing the variation of topology and Volta potential of the marked line before and after immersion.

trigger more localised corrosion around the Fe-rich intermetallic phase. But this is not happening in this case due to the uniform distribution of Cr.

No trenching behaviour was observed even after immersing the sample for 4 more hours for a total of 8 hrs in 0.1 M NaCl solution. Fiure 4.11 shows the SEM images of two regions after immersion for 8 hrs showing no trenching behaviour. But it is interesting to note the presence of bright spots on top of the Fe-rich intermetallic phase (red markings) denoting the phase is itself facing a corrosion attack leading to de-alloying of the phase [16, 17]. Further high resolution examination of these spots was not possible due to the limited resolution of the SEM-EDX instrument used in this research.

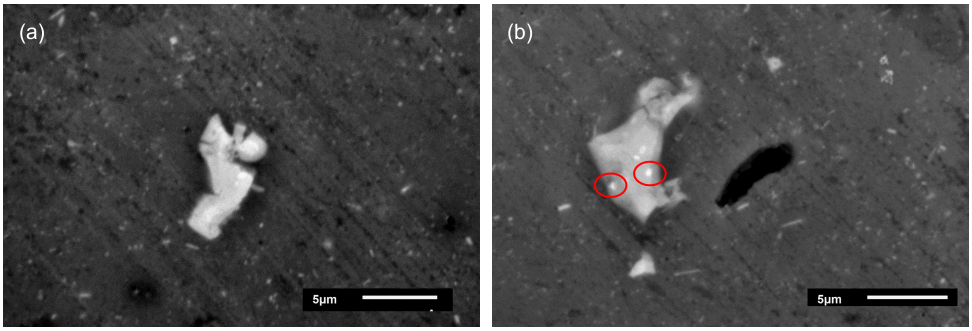

Figure 4.11: (a) and (b) shows two regions in AA5083 sample surface containing Fe-rich intermetallic phase showing no trenching after immersion for 8 hrs in 0.1 M NaCl solution

MG-SI INTERMETALLIC PHASES

Mg-Si intermetallic particles are known to shift from anodic character to cathodic character with respect to the Al matrix depending on the Mg content in the intermetallic phase. Initially the Mg-Si phase exhibit an anodic nature due to the higher Mg content. Due to its anodic nature, selective dissolution of Mg from the phase takes place leading to enrichment of Si content [31, 66]. This Si enrichment changes the anodic nature to cathodic nature of the Mg-Si intermetallic phase.

In this study the Mg-Si phase already shows a slight cathodic character before immersion. Red marking in 4.12 (a) shows the presence of Mg-Si phase and in figure 4.12 (b), the red marking shows a slight dip in Volta potential at the Mg-Si phase denoting a cathodic nature of the phase.

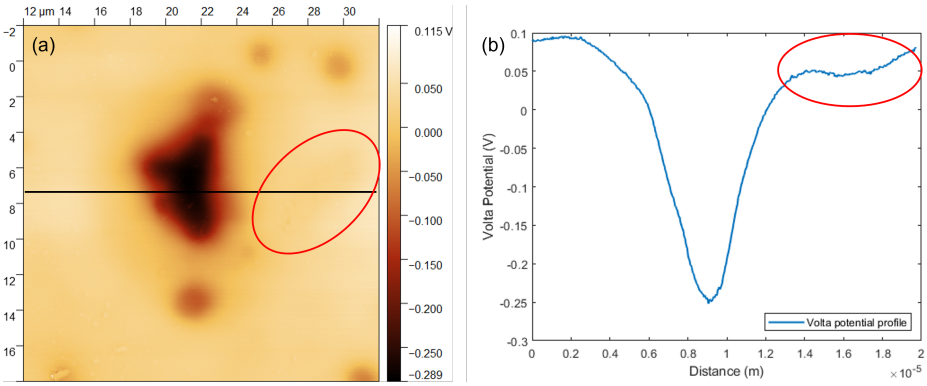

Figure 4.12: (a) Volta potential map of region containing both Fe-rich and Mg-Si intermetallic phase before immersion. (b) shows the line plot of the marked line in (a).

The selective dissolution of Mg can be clearly observed from the topology maps before and after immersion shown in figure 4.13 (a1) and (a2) respectively. The line profiles

before and after immersion shown in figure 4.13 (c) and (d) respectively represents a uniform material removal along the length of the Mg-Si phase leading to formation of craters. The depth of the crater formed is around 150 nm. K.A. Yasakau et al. [31] mentions that this depth won't exceed beyond few hundred nano meters range due to the formation of protective oxides of Mg which isolates the phase from further material dissolution.

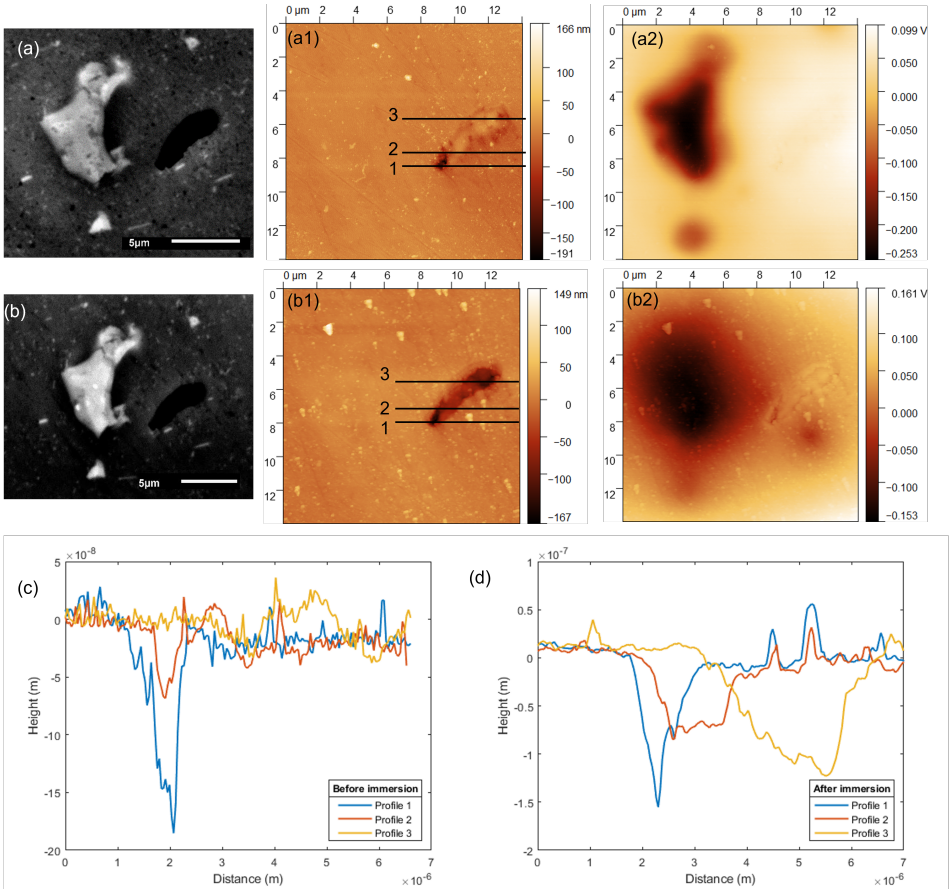

Figure 4.13: (a), (a1) and (a2) are the SEM image, topology map and the Volta potential map of both Fe-rich and Mg-Si intermetallic phase of AA5083 sample before immersion and (b), (b1) and (b2) are the counterparts after immersion in 0.1 M NaCl solution for 4 hrs. (c) and (d) are the plots showing the variation of topology of the marked line profiles before and after immersion.

4.3.2. INTERMETALLIC PHASES OF AA6082

FE-RICH INTERMETALLIC PHASES

Unlike the Fe-rich intermetallic phases in AA5083, the Fe-rich phases in AA6083 acts quite opposite in this 4 hrs immersion time frame. Within 4 hrs of immersion in 0.1 M NaCl solution, trenching of depth around 150 nm can be observed around the Fe-rich intermetallic phases of AA6082 sample. Refer to figure 4.14 (b1) and (c) which shows the topology map and the line profile showing trenching around the intermetallic phase after immerson respectively.

Further, unlike the Fe-rich intermetallic phases of AA5083 where the cathodic nature of the phase reduces after immersion, in AA6082, Fe-rich intermetallic phases shows an increase in cathodic nature after immersion. Refer to figure 4.14 (d) showing a increase in Volta potential in negative direction denoting an increase in cathodic nature of the intermetallic phase. This increase in cathodic nature suggests that the Fe-rich intermetallic phases of AA6082 enhances the galvanic coupling with the surrounding Al matrix which hence, is responsible for the formation of trench around the intermetalic phase.

Looking at the Volta potential profile at the Al matrix ends before and after immersion, a shift Al matrix to more anodic character (i.e. shift of Volta potential towards positive direction) can be observed. This shift makes more evident the enhancement of the cathodic activity of the Fe-rich intermetallic phase.

Apart from the change in the cathodic nature, by comparing the Volta potential maps before and after immersion (figure 4.14 (a2) and (b2) respectively), new active sites that did not exist initially can be observed. These new spots may correspond to the cathodic intermetallic phases lying just beneath the surface becomes active after immersion.

This increased activity of the Fe-rich intermetallic phases in AA6082 leading to trenching around the phase in this short immersion duration of 4 hrs may occur due to:

1. High concentration of Si localised in Fe-rich intermetallic phases and

2. No added protection from the oxides of Cr unlike AA5083

As Si is more cathodic with respect to Al, the localised presence of Si concentrated in Fe-rich intermetallic phases of AA6082 has the ability to increase the overall cathodic nature of the phase. Red markings in figure 4.14 (b) shows bright spots that are the result of internal de-alloying of the Fe-rich intermetallic phase. Internal de-alloying of the phase happens to the most anodic substance within the phase and in this case it is Al content inside the phase. As the Al de-alloys from the phase after immersion, the higher Si content in the phase will tend to further increase the cathodic nature of the phase.

Further, unlike AA5083, there is no Cr present in AA6083 samples and the additional protection from oxides of Cr is absent in AA6082 alloy.

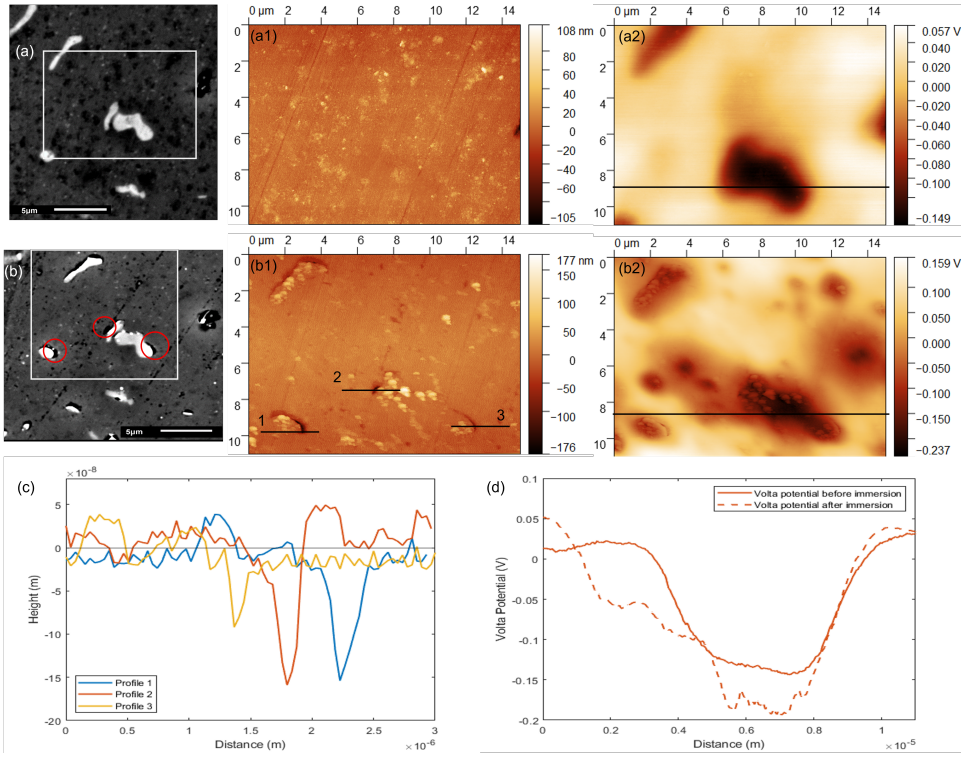

Figure 4.14: (a), (a1) and (a2) are the SEM image, topology map and the Volta potential map of Fe-rich intermetallic phase of AA6082 sample before immersion and (b), (b1) and (b2) are the counterparts after immersion in 0.1 M NaCl solution for 4 hrs. (c) and (d) are the plots showing the variation of topology of the marked line profiles before and after immersion.

MG-SI INTERMETALLIC PHASES

Mg-Si intermetallic phases of A6082 shows a very similar characteristics as the Mg-Si phases in AA5083. Observing the height profile of the phase initially before immersion in figure 4.15 (c), a small crater due to material dissolution can be observed. This also corresponds to initial selective leaching of Mg from the Mg-Si phase. The cathodic nature of the Mg-Si phase due to selective leaching of Mg and enrichment of Si is reflected in the Volta potential profile before immersion where a negative peak can be observed.

After immersion for 4 hrs in 0.1 M NaCl solution, the height profile shows a deeper crater formation but within around 100 nm depth and the corresponding Volta potential profile after immersion shows a flattened curve where the Volta potential at the phase is almost equal to that of the surrounding Al matrix. This denotes very low to no activity of the phase after certain amount of selective Mg leaching from the phase.

This also supports the findings of K.A. Yasakau et al. [31], where the inactivity of the Mg-Si phase, after certain amount of Mg leaching, is due to the formation of protective

Mg oxides.

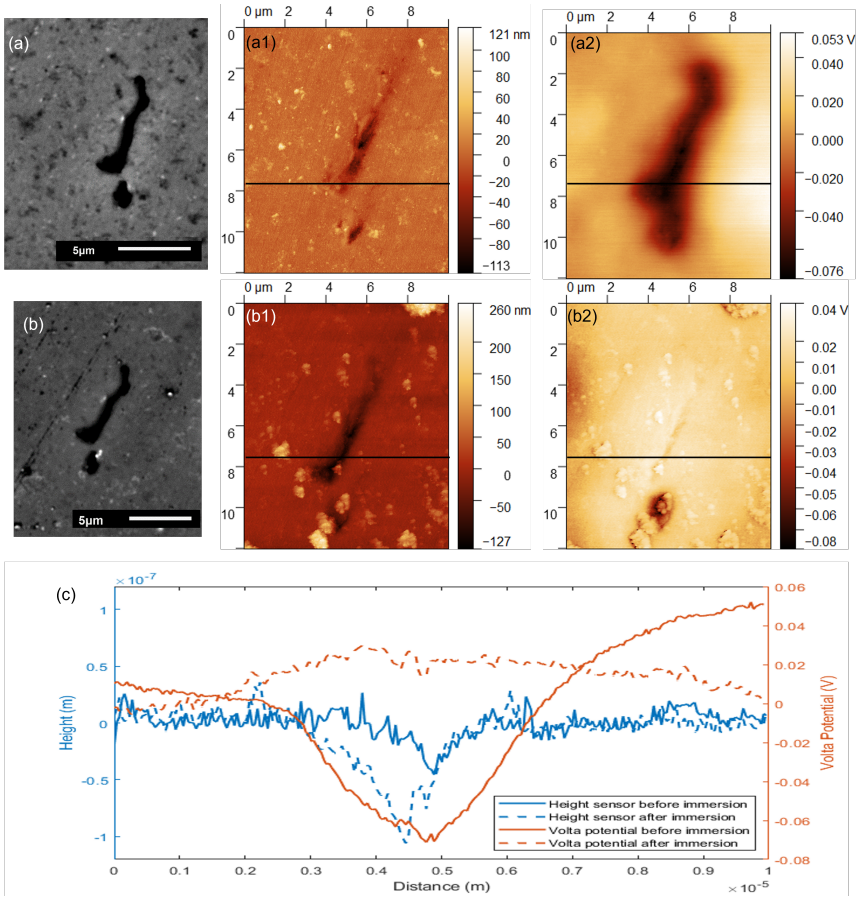

Figure 4.15: (a), (a1) and (a2) are the SEM image, topology map and the Volta potential map of Mg-Si intermetallic phase of AA6082 sample before immersion and (b), (b1) and (b2) are the counterparts after immersion in 0.1 M NaCl solution for 4 hrs. (c) shows the variation of topology indicating trenching from the marked line profiles 1, 2 and 3. (d) shows the Volta potential before and after immersion from the marked lines in respective Volta potential maps.

4.4. IN-SITU SURFACE ACTIVITY MONITORING

In this part of the research, SECM experiments were carried out to monitor in-situ surface activity of AA5083 and AA6082 alloys during immersion in a 0.1 M NaCl solution. By scanning selected areas of the surface with the high resolution SECM probe, it was possible to study the change in behaviour of surface containing IMPs during immersion. With this further conclusions regarding the effect of surface distribution of IMPs on the corrosion behaviour of the alloys were made.

Accoding to A. Aballe et al. [43], the surface distribution of $Al_6(Mn,Fe)$ intermetallic phase plays an important role in corrosion properties of the AA5083 alloy. The study mentions that, the higher the surface distribution of Fe-rich $Al_6(Mn,Fe)$ intermetallic phase decreased the pitting resistance (R_{pit}) leading to an increase in number of pit initiation. The susceptibility of corrosion of AA5083 alloy was mentioned to increases as the pit initiation on $Al_6(Mn,Fe)$ intermetallic phase increases.

In the current study, the surface distribution of cathodic intermetallic phases over the surface both AA5083 and AA6082 samples are analysed with the help of image analysis through ImageJ software [78] using SEM images of different areas of the sample surface. It is carried out to correlate with In-situ SECM surface activity maps to derive better conclusions on how surface distribution of intermetallic phases has a role in corrosion behaviour of the alloys.

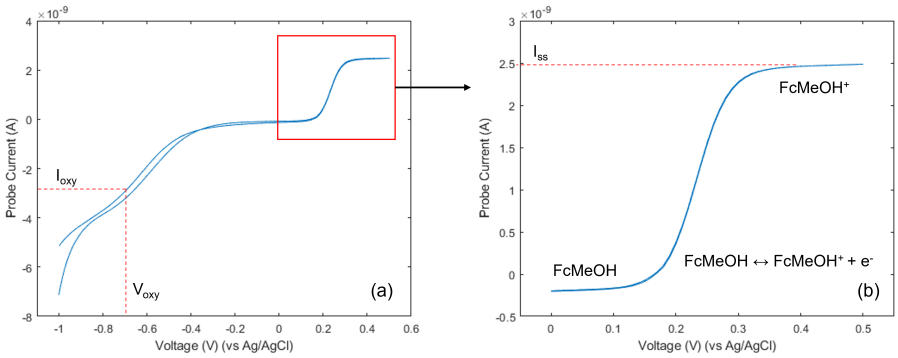

Figure 4.16: (a) Cyclic voltammetery in the voltage range of -1 V to 0.5 V showing bias voltage used for oxygen scans and the respective probe current and (b) cyclic voltammetery in 0 to 0.5 V range showing the redox reaction and the steady state current (I_{ss}) of 2 mM FcMeOH mediator in 0.1 M NaCl solution.

As mentioned in chapter 3, The surface activity was monitored by polarising the SECM probe at 0.5V (vs Ag/AgCl) for the oxidation of FcMeOH redox mediator and at -0.7V (vs Ag/AgCl) for the oxygen reduction. Refer to the voltammetery plots in figure 4.16 for the respective current values for FcMeOH oxidation and oxygen reduction. The output current values obtained for FcMeOH scan maps are normalised with respect to I_{ss} (refer to the equation 4.2). When the the current value at specific location is more than 1 denotes that the location is active and conductive whereas current values below 1

denotes a non-conductive nature of the location. For the oxygen scans, the direct probe current values are depicted, where if the absolute current value is less than 3 nA, it denotes that the location consumes oxygen and is cathodic with respect to the Al matrix.

$$Normalised\ Probe\ Output = \frac{Output\ Current}{I_{ss}} \tag{4.2}$$

4.4.1. SURFACE DISTRIBUTION OF CATHODIC INTERMETALLIC PHASES

Figure 4.17 shows the distribution of presence of cathodic particles/phases for the given size. The chosen area of examination is 300 × 300 μm at a magnification of ×300 for both the samples to obtain more reliable quantification. Further, the particles that are counted by the software to have size less than 600 nm are ignored because the chosen SEM image of 300 × 300 μm area may not be accurate in spotting such small features and the limitations in the resolution of SEM used might impart on the distribution. In addition to this, the image analysis from the ImageJ software also had noises in data when a larger area of SEM image is used.

From the histograms and the embedded tables (refer to 4.17), it can be observed that the mean size of the particles and the size range of the particles in AA5083 is higher compared with that of AA6082. This means that the percentage of particles that are larger in size has higher probability to be found in AA5083 than in AA6082. By calculations from the ImageJ software, it is found that the percentage of particles above 2.5 μm in size is about 12.60 % in AA5083 whereas in AA6082, it is only 1.14 %. This reflects the fact that the particles in A6082 are distributed in a smaller size range (0.5 - 3.5 μm) denoting more uniform size distribution compared to that of AA5083 (size range of 0.5 - 5.5 μm).

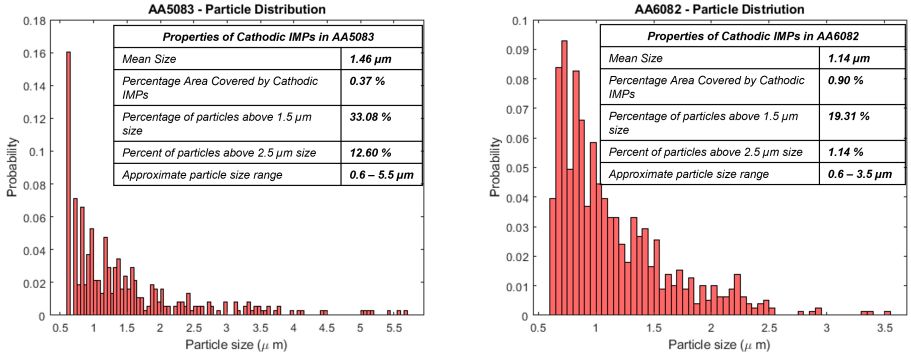

Figure 4.17: Cathodic particle size distribution of AA5083 and AA6082 alloy

Further, it is found that the total number of particles detected in the examined area for AA5083 is less than half the number of particles found in AA6083. Figure 4.1 is a good example to visually notice the difference in amount of bright contrast cathodic phases between AA5083 and AA6082 samples. Due to the large number of cathodic phases present in AA6082 samples, the area covered by these phases also is seen to be more

than twice the area covered in AA5083 samples.

4.4.2. SURFACE ACTIVITY OF AA5083 AND AA6082 ALLOY

The sequence of images in the left part and right part of the figure 4.18 shows the in-situ mapping of surface activity of AA5083 and AA6082 alloys respectively by SECM measurements using FcMeOH mediator. Observing the surface activities of both the sample surface at time 0 (as polished surface), it can be noted that the normalised probe output stays below 1. This indicates that both the samples are readily passivating exhibiting a non-conductive character [66] as soon as they encounter a corrosive environment. Further, as the immersion time increases, the probe output is observed to decrease which signifies that the activity of the surface is getting more passive over the time.

Even though the whole surface is passivating, it is know that the native oxide film on top of the intermetallic phases are weak compared to the rest of the Al matrix. This weakness in passive film formed on the intermetallic phases are reflected as peaks at specific spots as the presence of intermetallic phase will increase the reduction of $FcMeOH$ mediator and in turn increase the current output.

The differences in activity of these alloys can be clearly seen in the number of peaks as well as uniformity of the peaks observed in the SECM maps. It is evident from the time 0 map of AA5083 sample that the few peaks are largely isolated and shows a significant difference in peak intensities. Whereas for AA6082 at time 0, the number of peaks observed is comparatively higher which are located closer to each other and exhibit uniform peak intensities.

This differences in number of peaks and the uniformity can be well associated with the differences in distribution of intermetallic phases on the surface of these alloys. As the number of intermetallic phases and the total area covered by it is significantly low for AA5083 compared with AA6082, the number of peaks are less and are seen to be isolated far apart from each other. Whereas for AA6082, as the number and area covered by the intermetallic phases are comparatively higher, current peaks are observed closer to each other and in large number.

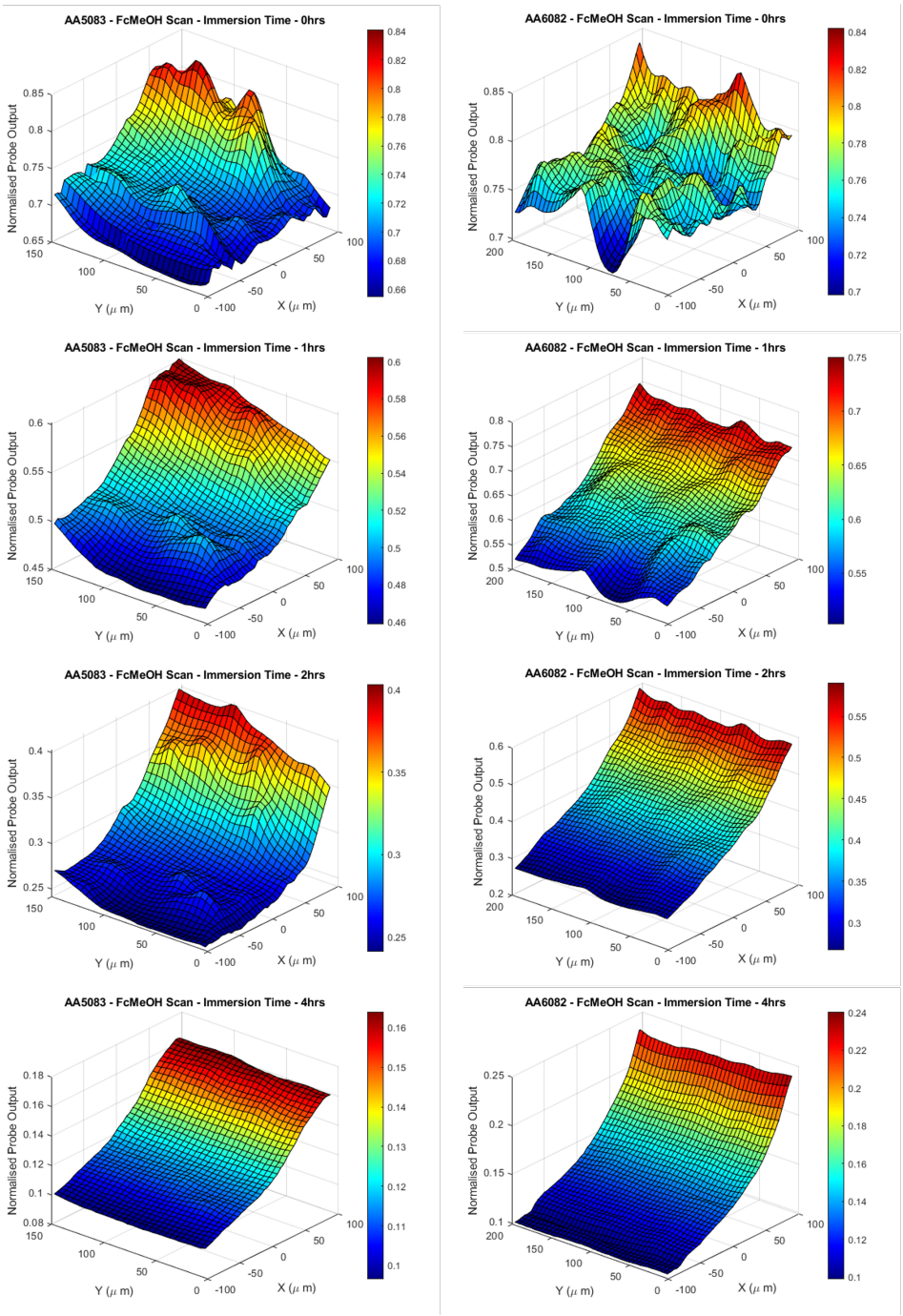

Figure 4.18: In-situ surface monitoring maps scanned every 1 hr for 4 hrs of immersion of AA5083 (Left) and AA682 (Right) samples.

PASSIVE FILM BREAKDOWN

Interestingly in AA6082, even though most regions of the surface are passive, at certain regions the peak normalised output is seen to exceed unity after immersion. Figure 4.19 shows the progression of surface activity along immersion time of a very active region in AA6082 sample. It can be observed at time 0 that almost the whole region shows a very conductive character denoting the passive layer is very weak overall due to the crowded presence of intermetallic phases.

Later after 1 hr immersion time, the same region can be observed to having probe output less than unity. This denotes that the passive layer is getting stronger in suppressing the active regions. Further immersion for one more hour, at 2hr immersion time, spots of the surface can be seen to show a very high probe output peaks (normalised probe output > 2). These spots of very high probe output can denote a breakdown in passive film leading to initiation of pit into the alloy surface and severe material dissolution.

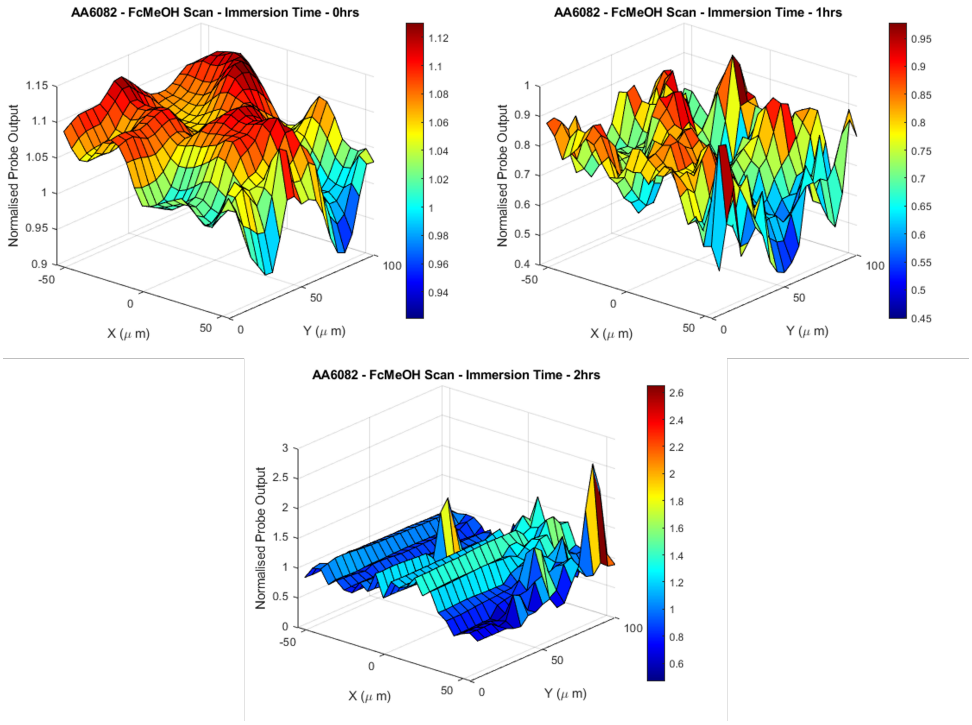

Figure 4.19: In-situ SECM map of a relatively active region in AA6082 sample surface showing passive layer breakdown after 2 hrs of immersion in 0.1 M NaCl solution.

It is also interesting to note the background signals in the SECM map after 2 hrs immersion in figure 4.19 where the regions apart from the peaks i.e the background signals,

also shows probe output more than unity. This shows that even though the passive layer breakdown seems to be localised to few spots, the overall activity of the surrounding region is also increased showing that the passive layer is affected in a larger extent.

This kind of passive layer breakdown is not observed in the time frame of these experiment denoting that AA5083 is better passivating compared with AA6082. This passivating behaviour, as already mentioned, could be due to the presence of Cr uniformly distributed all over the surface.

4.4.3. OXYGEN SCAN

The oxygen scanning was carried out at time 0 after the FcMeOH scan to differentiate the cathodic and anodic intermetallic phases by scanning the oxygen consumption. A (negative) peak in the SECM maps denotes that the oxygen consumption is high at that region.

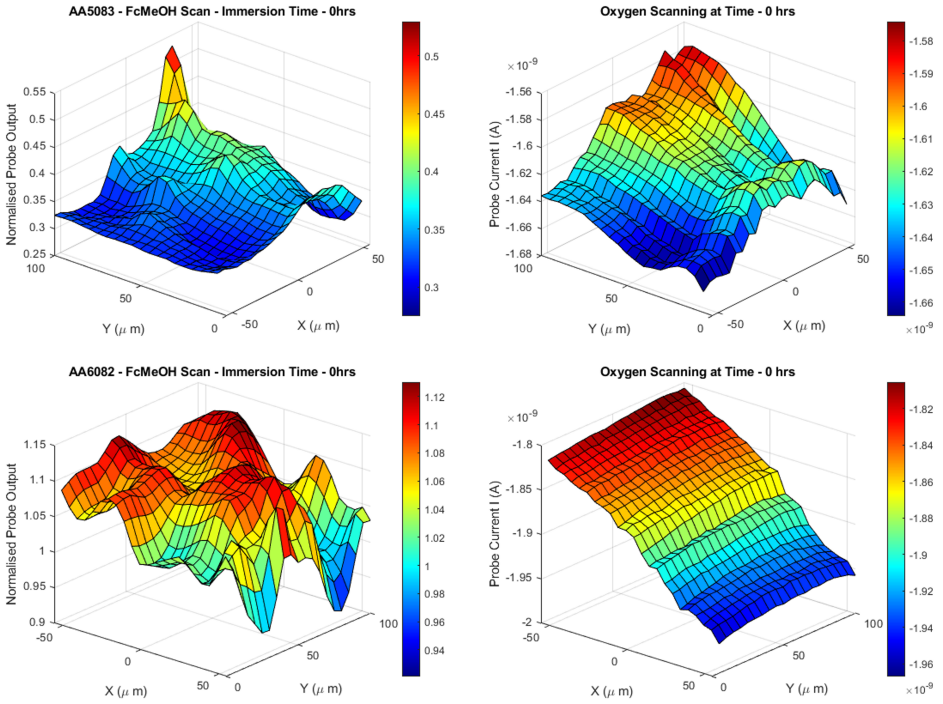

Figure 4.20: FcMeOH scan maps (left) and its corresponding Oxygen scan maps of AA5083 and AA6082 samples.

Figure 4.20 shows a FcMeOH scan of a region in AA5083 and AA6082 alloy on the left and its corresponding oxygen scans of the same region on the right. Both the oxygen scan images show higher oxygen consumption all over the region where the absolute values of the measured probe current is less than 3 nA. This denotes that the surface on

a whole shows a very cathodic character and the oxygen consumption happens all over the surface.

Apart from this, no solid conclusions can be made regarding the type of intermetallic phases present. The surface maps shows almost a flat signal all over the surface exhibiting no significant relevance to the existing peaks in FcMeOH scans. This arises questions whether the oxygen scan is really useful to draw any conclusions or not. To answer this question, first it's necessary to find why the oxygen scan shows a flat signal all over the surface and why it is unable to differenciate the intermetallic phases.

The flat signal might be due to the way the oxygen is getting consumed by the intermetallic phase and the influence of operating distance. The cathodic intermetallic phase consumes oxygen from a volume of electrolyte present on top of it. Due to persistent deposition of corrosion products on the probe surface after each scan made erroneous subsequent scans. To avoid this, the working distance of initial 10-15 μm is increase to 20-25 μm. Due to the increased operating distance, the probe reflects the oxygen availability from a larger volume leading to a reduced clarity compared to the situation when the probe is close to the surface which helps it to reflect the oxygen availability localised to the intermetallic phase.

Even then, if measures are taken to keep the working distance small, for the case of AA5083 and AA6082 samples, differentiating cathodic and anodic phases is still difficult due to the varying character of Mg-Si phase from being anodic to cathodic by selective dissolution of Mg and enrichment of Si in it. It is also shown in figure 4.12 and 4.15 that even before immersion, Mg-Si phase shows a cathodic behaviour. And Zheng et al. [66] shows that Mg-Si phase exhibits a cathodic behaviour as strong as the Fe-rich intermetallic phases in Al-Mg-Si alloy. In this case, since both Fe-rich intermetallic phase and Mg-Si phase exhibits a cathodic nature, using an oxygen scan and trying to differentiate them makes depending on their cathodic and anodic nature makes no sense.

4.5. DISCUSSION

Combining the potentiodynamic polarisation curves with the results from particle distribution and in-situ SECM for AA5083 and AA6082, interesting correlations can be understood which help in understanding the localised corrosion of these alloys. Figure 4.21 shows the PDP curves of AA5083 and AA6082 sample in 0.1 M NaCl solution.

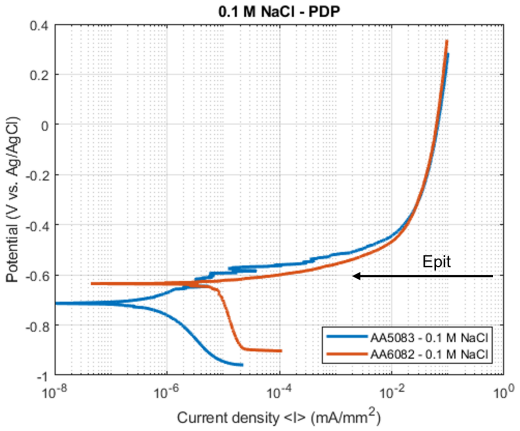

Figure 4.21: Potentiodynamic polarisation plot of AA5083 and AA6082 samples in 0.1 M NaCl solution. The figure also represents roughly the pitting potential for AA5083 sample.

4.5.1. EFFECT OF ALLOY COMPOSITION

From figure 4.21 AA6082 can be observed to exhibit negligible resistance to pitting (R_{pit}) whereas it is comparatively large for AA5082 alloy. Higher R_{pit} denotes that the alloy offers a good resistance to stable pit growth. Further, the pitting potential (E_{pit}) depends on the composition of the Al alloy where the alloying elements contribute in forming better passive layer [79–82]. Rama B. Inturi and Z. Szklarska-Smialowska [79, 80] mentions that there exists a relation between the E_{pit} of the alloy and the solubility of oxides formed by the alloying elements where the E_{pit} increased as the solubility of the oxides of alloying elements decreases.

AA5083 is seen to be comparatively passivating than AA6082 where the Volta potential of AA5083 is seen to be getting less cathodic with immersion whereas the cathodicity increases with immersion in AA6082 (refer to figure 4.10 and figure 4.14). This behaviour can be well correlated with the findings mentioned above where the passivating behaviour is associated with the additional presence of alloying elements especially Cr.

Figure 4.22 shows the elemental mapping of a region in AA5083 sample containing both Fe-rich and Mg-Si intermetallic phase where near uniform distribution of Cr is observed irrespective of intermetallic phase or the Al matrix. The protective nature of Cr is also well reflected in PDP curves where comparatively higher R_{pit} in AA5083 (refer to figure 4.21) is observed. This additional protection is absent in AA6082 alloy and hence

it shows a immediate pitting (negligible R_{pit}) as it is polarised.

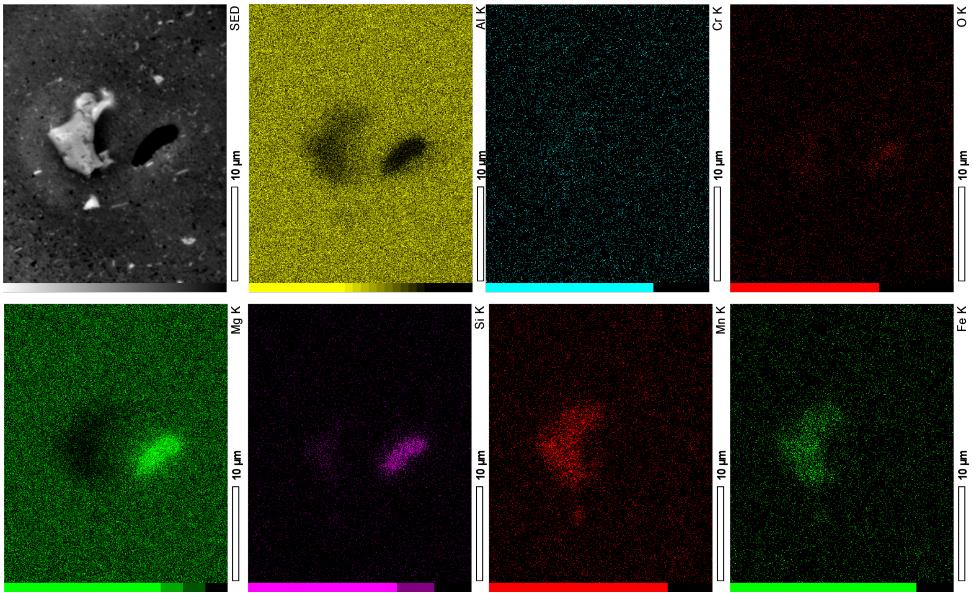

Figure 4.22: EDX spectroscopy elemental maps of a region in AA5083 sample surface containing both Fe-rich and Mg-Si intermetallic phase. The blue coloured map corresponds to Cr content in the region.

4.5.2. EFFECT OF PARTICLE SIZE AND DISTRIBUTION

In addition to the higher pitting resistance (R_{pit}), metastable pitting events can also be observed in AA5083 PDP curves but not in AA6082. R.K. Gupta et al. [27] mentions that the presence of very small inclusions or intermetallic phases in nano meter sizes and the electrochemical heterogeneity of the alloy has a positive influence in metastable pitting characteristics of the alloy.

The Ti particles in AA5083 can be seen to form trenches of size 1 - 2 μm (see figure 4.23) and this size is consistently observed not only in immersion but also in polarised surfaces from UPW, ACW and 0.1 M NaCl solutions (refer to figures 4.6 and 4.7 (b)). In contrast to the case of AA5083, figure 4.23 (b) shows the surface of AA6082 after immersion for 4hrs in 0.1 M NaCl solution, where almost all the Fe-rich intermetallic phases are observed to form trench around them. Comparing this behaviour of AA5083 and AA6082, it is clear that the pit initiation in AA5083 is on Ti particles whereas it is the Fe-rich intermetallic phases for AA6083.

The Ti particles in AA5083 are also seen to form a black oxide over the trenched surface (see figure 4.23(a)) denoting a passivating behaviour. Futher, the majority of the Ti particles are also seen to be still intact to the Al matrix showing that the formed trench is arrested from growing enough for the particle to fall out of the formed pit. These observations combined with the small size of the Ti particles shows that the Ti particles

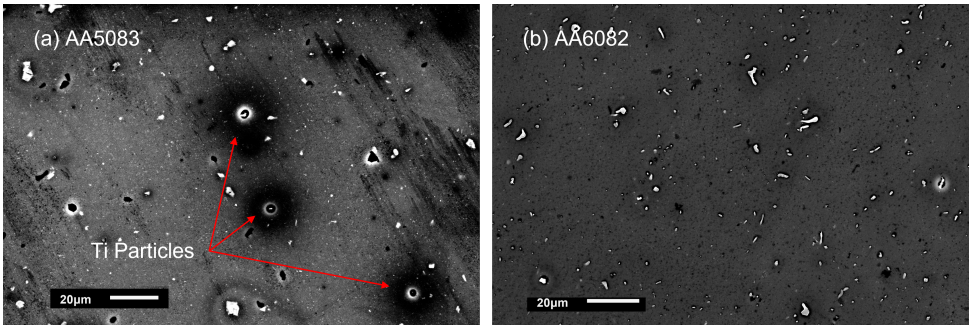

Figure 4.23: SEM image of (a) AA5083 sample showing trenchig around the Ti particles and (b) AA6082 sample showing that the trench is happening around almost all the Fe-rich intermetallic phases.

has a significant role in the metastable pitting events observed in AA5083. Further, the cathodic character of the Ti particle combined with the existance of the intermetallic phases in broarder size ranges contributes well enough to the electrochemical heterogeneity of the alloy resulting in promotion of metastable pitting [27, 83].

Allthough the pit initiation is at Ti particles in A5083, the propagation of pit is observed predominantly through Fe-rich intermetallic phases as the Ti particles gets passivated quickly. In the case of AA6082, both initiation and propagation of pits are observed in Fe-rich intermetallic phases (refer to figure 4.23 (b)). The combined effect of high number density of intermetallic phases, its existing in small size range and comparatively homogeneous electrochemical characteristics due to these factors result in uniform pit initiation in almost all the Fe-rich intermetallic phases followed by stable pit propagation. Due to which, no metastable pitting events are seen in the polarisation curves of AA6082.

4.5.3. LOCALISED CORROSION BEHAVIOUR OF AA5083 AND AA6082

In AA5083 samples it is found that the number and area covered by the cathodic intermetallic particles are comparitively lower. The pit initiation happens at Ti particles. On top of the cathodic nature of Ti particles, due to the availability of larger anodic area (Al matrix) for the size of Ti particles, these particles tend to have more drive for corrosion initiation.

Allthough the initiation is at Ti particles, the trench formed around Ti particles is not seen as the major site for pit propagation. The trenches gets passivated quickly and gets dormant. Due to the protective nature of oxides of Cr, the alloy is well passivated and hence, it's difficult for pit to initiate at Fe-rich intermetallic phases. Further polarisation is required to the breakdown of the protective oxide layer and initiates pits at Fe-rich intermetallic phases. These pits are observed to grow further. Refer to figure 4.24 (a) for the schematic of localised pit initiation in AA5083 samples.

For the case of AA6082, the cathodic intermetallic phases are higher in number, has

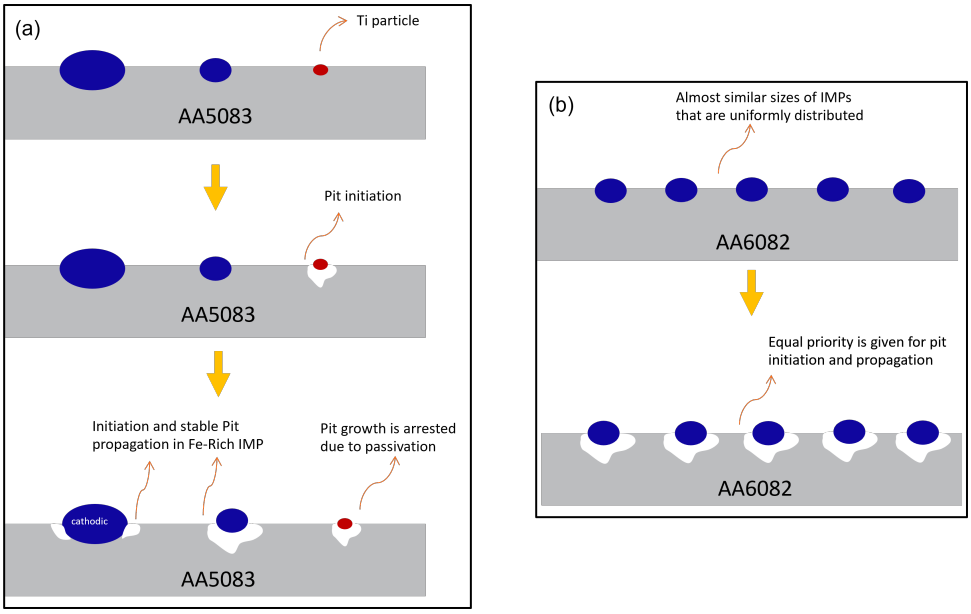

Figure 4.24: Schemtaic representation of the initiation and subsequent progression of localised corrosion process in (a) AA5083 sample and (b) AA6082 sample.

uniform size and distribution and are of the same type (Fe-rich). Due to the similarity in type and sizes, the intermetallic phases have similar galvanic coupling with the Al matrix. In addition to this, the availability of anodic area is also equally distributed amongst all the intermetallic phases due to its uniform size and distribution.

These factors provides equal priority for almost all the Fe-rich intermetallic phases in AA6082 to form pits equally and the initiated pits are observed to grow as there is no passivation seen in this alloy. Further, the breakdown of passive layer is quite faster in AA6082 due to the absence of additional protection from Cr. This quicker passive layer breakdown in AA6082 compared with that of A5083 can be confirmed by the in-situ SECM results of passive layer breakdown in AA6082 (refer to figure 4.19). Refer to figure 4.24 (b) for the schematic of localised pit initiation in AA6082 samples.

Finally, even though the mechanism of localised pit initiation explained above is obtained from the results of immersion and polarisation tests in 0.1 M NaCl solution, these observations can be well correlated with UPW and ACW conditions. From the polarisation curves (refer to 4.4), it is interesting to note the metastable pitting also exists in UPW and ACW conditions for AA5083 but not for AA6082 proving the effect of Ti particles in it. The major difference observed is the pitting propagation where a sudden increase in current density is found predominantly in 0.1 M NaCl condition. It is known that in the presence of Cl^- ions, the corrosion process is aggravated by severe pitting. Since, the UPW and ACW contains no and very low concentration of Cl^- ions respectively, no se-

vere pitting (sudden increase in current density) is observed in these conditions.

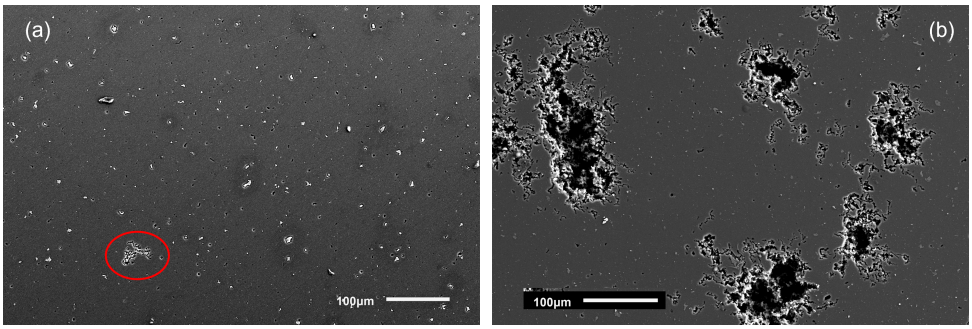

Figure 4.25: SEM images of AA5083 sample after polarisation in (a) UPW conditions and (b) 0.1 M NaCl condition.

Figure A.3 acts as a good example to show the effect of presence of Cl^- ions. The similarity observed is that the way the pit spreads on the surface of the sample. A branched fashion of pit spreading can be observed in both the cases. This shows that the trenches developed around the intermetallic phases grows and connects with other trenches in proximity to for a branched like pit spreading. In the case of UPW (figure A.3 (a)), the red marking shows one of the very few spots showing a pit spreading whereas in the case of 0.1 M NaCl solution figure A.3 (b)), in addition to spreading to a very large extent, deep propagation of pits are observed. The deeper propagation of pit is a general outcome expected with the presence of Cl^- ions.

5

CONCLUSIONS AND FUTURE RECOMMENDATIONS

The following conclusions can be drawn based on the above results obtained:

- AA5083 and AA6082 alloys have 2 major groups of intermetallic phases; Fe-rich and Mg-Si intermetallic phases. Fe-rich intermetallic phases acts cathodic with respect to the Al matrix. The Mg-Si intermetallic phases previously reported to act both anodic and cathodic depending on its Mg content but in this study it is measured and observed to be cathodic with respect to the Al matrix.

- Cathodic nature of Fe-rich intermetallic phases initiates corrosion by dissolving the Al matrix around it whereas the Mg-Si phase selectively dissolves the most anodic element (Mg) in it leading to Si enrichment. Fe-rich intermetallic phases are observed to form deeper trenches whereas Mg-Si phase is observed to get inactive overtime due to deposition of oxides of Mg on it.

- The formed trenches when in close proximity, connects to form a branched shaped pit. In the presence of corrosive ions like Cl^-, the ions flows into the initiated pits to fuel the pits to propagate deeper. However in the case of no corrosive ions, the corrosion process is very slow and the pits gets passivated quickly due time.

- There is no significant difference observed in the behaviour of Mg-Si in 0.1 M NaCl solution between AA5083 and AA6082 alloy. But Fe-rich intermetallic phases are seen to form trenches much sooner in AA6082 compared with A5082 alloy.

- Alloy composition has a significant effect on the localised corrosion behaviour. Additional content of elements like Cr which forms less soluble oxides helps in forming stronger passive layers that are difficult to break to initiate pit formation. The passive layer also increases the resistance to pitting R_{pit} and hence it requires further polarisation to break the passive layer.

- The size and distribution of intermetallic phases also play an important role in localised corrosion. Small particles like Ti in AA5083 which exhibits strong cathodic character with respect to the base matrix are responsible for the corrosion initiation in AA5083 alloy. The higher the surface coverage and the number of cathodic intermetallic phases increases the susceptibility of localised corrosion of the alloy. Further, the initiation of corrosion is expected to start from the small sized intermetallic phases as the availability of anodic area is much higher for small sized particles which drive the corrosion.

This study made significant contributions to understand the localised corrosion activity and the role of intermetallic phases in it through localised methods like AFM-SKPFM and in-situ SECM techniques. This study emphasis on the effect of alloying elements and the surface distribution of the cathodic intermetallic phases on the localised corrosion initiation. It also suggests a sequential idea of how and where the localised pit initiates and then propagates.

However, this study cannot be sufficient to completely understand the overall corrosion behaviour of these alloys. Following are the future recommendations for this study:

- Additional polarisation studies to prove the way of pit initiation turning to deeper propagation by analysing samples polarised to an increase step of voltage. Details of sequential pit popogation can be obtained and observed.
- Study the localised corrosion of the samples for longer immersion time to have a better understanding on how the propagation of the pit happens.
- Perform in-situ SECM studies under polarisation of the sample to better elucidate the surface activity of the samples.
- Screening and analysing methods like inhibitors to prevent the corrosion initiation.
- Using a setup that accommodates the flow of solution to simulate the actual scenario in ASML cooling channels.

A

APPENDIX

A.1. IMAGE J ANALYSIS OF SEM IMAGES

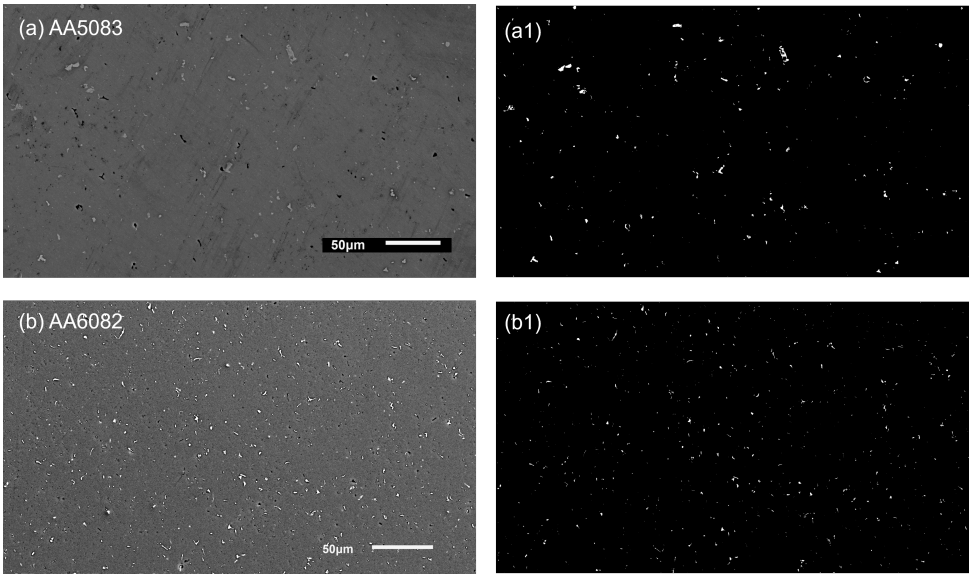

Figure A.1: SEM images of (a) AA5083 and (b) AA6082 sample surface and its corresponding (a1) and (b1) binary mapping of highlighting the cathodic intermetallic particles. The is a stark difference between the two samples in the size and distribution of intermetallic phases.

A

A.2. ADDITIONAL IN-SITU SECM MAPS

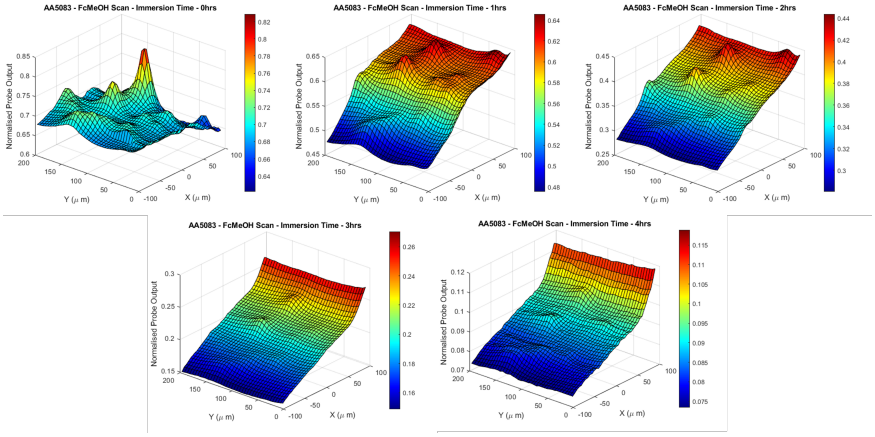

Figure A.2: In-situ SECM surface activity maps of AA5083 surface at different immersion time frames.

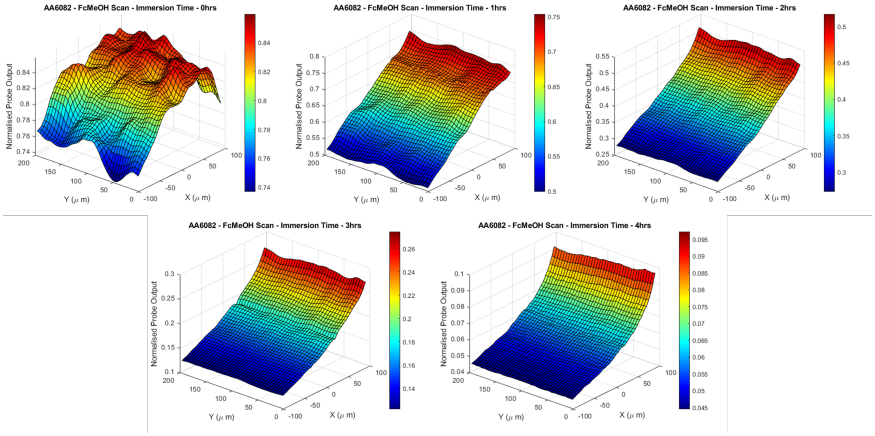

Figure A.3: In-situ SECM surface activity maps of AA6082 surface at different immersion time frames.

BIBLIOGRAPHY

[1] "Definition and Importance of Corrosion". In: *Corrosion and Corrosion Control*. John Wiley and Sons, Ltd, 2008. Chap. 1, pp. 1–8. ISBN: 9780470277270. DOI: https://doi.org/10.1002/9780470277270.ch1.

[2] George V. Chilingar, Ryan Mourhatch, and Ghazi D. Al-Qahtani. "CHAPTER 8 - ECONOMICS OF CORROSION". In: *The Fundamentals of Corrosion and Scaling for Petroleum and Environmental Engineers*. Ed. by George V. Chilingar, Ryan Mourhatch, and Ghazi D. Al-Qahtani. Gulf Publishing Company, 2008, pp. 209–221. ISBN: 978-1-933762-30-2. DOI: https://doi.org/10.1016/B978-1-933762-30-2.50014-8.

[3] C.M. Hansson. "1 - An introduction to corrosion of engineering materials". In: *Corrosion of Steel in Concrete Structures*. Ed. by Amir Poursaee. Oxford: Woodhead Publishing, 2016, pp. 3–18. ISBN: 978-1-78242-381-2. DOI: https://doi.org/10.1016/B978-1-78242-381-2.00001-8.

[4] Carolyn M Hansson. "The impact of corrosion on society". In: *Metallurgical and Materials Transactions A* 42.10 (2011), pp. 2952–2962.

[5] Robert R Schaller. "Moore's law: past, present and future". In: *IEEE spectrum* 34.6 (1997), pp. 52–59.

[6] AS Standard et al. "Standard Guide for Ultra Pure Water Used in the Electronics and Semiconductor Industries". In: (2013).

[7] Ray Collier Hughes, PC Mürau, and Gordon Gundersen. "Ultrapure water. Preparation and quality". In: *Analytical Chemistry* 43.6 (1971), pp. 691–696.

[8] LA Melnik and DA Krysenko. "Ultrapure water: properties, production, and use". In: *Journal of Water Chemistry and Technology* 41.3 (2019), pp. 143–150.

[9] P. Rambabu, N. Eswara Prasad, V. V. Kutumbarao, and R. J. H. Wanhill. "Aluminium Alloys for Aerospace Applications". In: *Aerospace Materials and Material Technologies : Volume 1: Aerospace Materials*. Ed. by N. Eswara Prasad and R. J. H. Wanhill. Singapore: Springer Singapore, 2017, pp. 29–52. ISBN: 978-981-10-2134-3. DOI: 10.1007/978-981-10-2134-3_2.

[10] Omid Ferdowsi Hosseinabadi and Mohammad Reza Khedmati. "A review on ultimate strength of aluminium structural elements and systems for marine applications". In: *Ocean Engineering* 232 (2021), p. 109153. ISSN: 0029-8018. DOI: https://doi.org/10.1016/j.oceaneng.2021.109153.

[11] Jürgen HIRSCH. "Recent development in aluminium for automotive applications". In: *Transactions of Nonferrous Metals Society of China* 24.7 (2014), pp. 1995–2002. ISSN: 1003-6326. DOI: https://doi.org/10.1016/S1003-6326(14)63305-7.

A

[12] Yiğit Türe and Cengiz Türe. “An assessment of using Aluminum and Magnesium on CO2 emission in European passenger cars”. In: *Journal of Cleaner Production* 247 (2020), p. 119120. ISSN: 0959-6526. DOI: https://doi.org/10.1016/j.jclepro.2019.119120.

[13] K.A. Yasakau, M.L. Zheludkevich, and M.G.S. Ferreira. “15 - Role of intermetallics in corrosion of aluminum alloys. Smart corrosion protection”. In: *Intermetallic Matrix Composites*. Ed. by Rahul Mitra. Woodhead Publishing, 2018, pp. 425–462. ISBN: 978-0-85709-346-2. DOI: https://doi.org/10.1016/B978-0-85709-346-2.00015-7.

[14] Shouxun Ji, Wenchao Yang, Feng Gao, Douglas Watson, and Zhongyun Fan. “Effect of iron on the microstructure and mechanical property of Al–Mg–Si–Mn and Al–Mg–Si diecast alloys”. In: *Materials Science and Engineering: A* 564 (2013), pp. 130–139. ISSN: 0921-5093. DOI: https://doi.org/10.1016/j.msea.2012.11.095.

[15] N. Birbilis and R. G. Buchheit. “Electrochemical Characteristics of Intermetallic Phases in Aluminum Alloys: An Experimental Survey and Discussion”. In: *Journal of The Electrochemical Society* 152.4 (Mar. 2005), B140. DOI: 10.1149/1.1869984.

[16] A. Kosari, H. Zandbergen, F. Tichelaar, P. Visser, P. Taheri, H. Terryn, and J.M.C. Mol. “In-situ nanoscopic observations of dealloying-driven local corrosion from surface initiation to in-depth propagation”. In: *Corrosion Science* 177 (2020), p. 108912. ISSN: 0010-938X. DOI: https://doi.org/10.1016/j.corsci.2020.108912.

[17] A. Kosari, F. Tichelaar, P. Visser, H. Zandbergen, H. Terryn, and J.M.C. Mol. “Dealloying-driven local corrosion by intermetallic constituent particles and dispersoids in aerospace aluminium alloys”. In: *Corrosion Science* 177 (2020), p. 108947. ISSN: 0010-938X. DOI: https://doi.org/10.1016/j.corsci.2020.108947.

[18] Christian Vargel. “Chapter B.1 - The corrosion of aluminium”. In: *Corrosion of Aluminium (Second Edition)*. Ed. by Christian Vargel. Second Edition. Amsterdam: Elsevier, 2020, pp. 41–61. ISBN: 978-0-08-099925-8. DOI: https://doi.org/10.1016/B978-0-08-099925-8.00008-9.

[19] E. Ghali. “Aluminum and Aluminum Alloys”. In: *Uhlig’s Corrosion Handbook*. John Wiley Sons, Ltd, 2011. Chap. 54, pp. 715–745. ISBN: 9780470872864. DOI: https://doi.org/10.1002/9780470872864.ch54.

[20] “Thermodynamics: Pourbaix Diagrams”. In: *Corrosion and Corrosion Control*. John Wiley Sons, Ltd, 2008. Chap. 4, pp. 43–51. ISBN: 9780470277270. DOI: https://doi.org/10.1002/9780470277270.ch4.

[21] K. Lutton Cwalina, C.R. Demarest, A.Y. Gerard, and J.R. Scully. “Revisiting the effects of molybdenum and tungsten alloying on corrosion behavior of nickel-chromium alloys in aqueous corrosion”. In: *Current Opinion in Solid State and Materials Science* 23.3 (2019), pp. 129–141. ISSN: 1359-0286. DOI: https://doi.org/10.1016/j.cossms.2019.03.002.

[22] Abraham A. Becerra Araneda, Mariano A. Kappes, Martín A. Rodríguez, and Ricardo M. Carranza. “Pitting corrosion of Ni-Cr-Fe alloys at open circuit potential in chloride plus thiosulfate solutions”. In: *Corrosion Science* 198 (2022), p. 110121. ISSN: 0010-938X. DOI: https://doi.org/10.1016/j.corsci.2022.110121.

[23] B. Zhang and X.L. Ma. "A review—Pitting corrosion initiation investigated by TEM". In: *Journal of Materials Science Technology* 35.7 (2019), pp. 1455–1465. ISSN: 1005-0302. DOI: https://doi.org/10.1016/j.jmst.2019.01.013.

[24] "Review of micro-scale and atomic-scale corrosion mechanisms of second phases in aluminum alloys". In: *Transactions of Nonferrous Metals Society of China* 31.11 (2021), pp. 3205–3227. ISSN: 1003-6326. DOI: https://doi.org/10.1016/S1003-6326(21)65727-8.

[25] Christian Vargel. "Chapter C.2 - Pitting corrosion". In: *Corrosion of Aluminium (Second Edition)*. Ed. by Christian Vargel. Second Edition. Amsterdam: Elsevier, 2020, pp. 163–183. ISBN: 978-0-08-099925-8. DOI: https://doi.org/10.1016/B978-0-08-099925-8.00014-4.

[26] G. S. Frankel. "Pitting Corrosion of Metals: A Review of the Critical Factors". In: *Journal of The Electrochemical Society* 145.6 (June 1998), p. 2186. DOI: 10.1149/1.1838615.

[27] R.K. Gupta, N.L. Sukiman, M.K. Cavanaugh, B.R.W. Hinton, C.R. Hutchinson, and N. Birbilis. "Metastable pitting characteristics of aluminium alloys measured using current transients during potentiostatic polarisation". In: *Electrochimica Acta* 66 (2012), pp. 245–254. ISSN: 0013-4686. DOI: https://doi.org/10.1016/j.electacta.2012.01.090.

[28] Robert A. Sielski. "Research needs in aluminum structure". In: *Ships and Offshore Structures* 3.1 (2008), pp. 57–65. DOI: 10.1080/17445300701797111.

[29] J R Davis. "Corrosion of aluminum and aluminum alloys". In: (Jan. 1999). URL: https://www.osti.gov/biblio/6434981.

[30] Mary Lyn C. Lim, Robert G. Kelly, and John R. Scully. "Overview of Intergranular Corrosion Mechanisms, Phenomenological Observations, and Modeling of AA5083". In: *Corrosion* 72.2 (Nov. 2015), pp. 198–220. ISSN: 0010-9312. DOI: 10.5006/1818.

[31] Kiryl A. Yasakau, Mikhail L. Zheludkevich, Sviatlana V. Lamaka, and Mario G.S. Ferreira. "Role of intermetallic phases in localized corrosion of AA5083". In: *Electrochimica Acta* 52 (27 Oct. 2007), pp. 7651–7659. ISSN: 00134686. DOI: 10.1016/j.electacta.2006.12.072.

[32] Tamara Radetić, Miljana Popović, and Endre Romhanji. "Microstructure evolution of a modified AA5083 aluminum alloy during a multistage homogenization treatment". In: *Materials Characterization* 65 (Mar. 2012), pp. 16–27. ISSN: 10445803. DOI: 10.1016/j.matchar.2011.12.006.

[33] U. Donatus, G. E. Thompson, X. Zhou, J. Wang, A. Cassell, and K. Beamish. "Corrosion susceptibility of dissimilar friction stir welds of AA5083 and AA6082 alloys". In: *Materials Characterization* 107 (2015), pp. 85–97. DOI: 10.1016/j.matchar.2015.07.002.

[34] L. Tan and T. R. Allen. "Effect of thermomechanical treatment on the corrosion of AA5083". In: *Corrosion Science* 52 (2 Feb. 2010), pp. 548–554. ISSN: 0010938X. DOI: 10.1016/j.corsci.2009.10.013.

A

[35] S. Jain, J.L. Hudson, and J.R. Scully. “Effects of constituent particles and sensitization on surface spreading of intergranular corrosion on a sensitized AA5083 alloy”. In: *Electrochimica Acta* 108 (Oct. 2013), pp. 253–264. ISSN: 00134686. DOI: 10.1016/j.electacta.2013.06.036.

[36] E. F. Abo Zeid. “Mechanical and electrochemical characteristics of solutionized AA 6061, AA6013 and AA 5086 aluminum alloys”. In: *Journal of Materials Research and Technology* 8.2 (2019), pp. 1870–1877. ISSN: 2238-7854. DOI: https://doi.org/10.1016/j.jmrt.2018.12.014.

[37] D.J Chakrabarti and David E Laughlin. “Phase relations and precipitation in Al–Mg–Si alloys with Cu additions”. In: *Progress in Materials Science* 49.3 (2004). A Festschrift in Honor of T. B. Massalski, pp. 389–410. ISSN: 0079-6425. DOI: https://doi.org/10.1016/S0079-6425(03)00031-8.

[38] Letian Fan, Jijun Ma, Chengxiong Zou, Jun Gao, Haisheng Wang, Jing Sun, Quanmei Guan, Jun Wang, Bin Tang, Jinshan Li, and William Yi Wang. “Revealing foundations of the intergranular corrosion of 5XXX and 6XXX Al alloys”. In: *Materials Letters* 271 (2020), p. 127767. ISSN: 0167-577X. DOI: https://doi.org/10.1016/j.matlet.2020.127767.

[39] Christian Vargel. *Corrosion of Aluminium*. 2004, pp. 1–626. ISBN: 9780080444956. DOI: 10.1016/B978-0-08-044495-6.X5000-9.

[40] W. J. Liang, P. A. Rometsch, L. F. Cao, and N. Birbilis. “General aspects related to the corrosion of 6xxx series aluminium alloys: Exploring the influence of Mg/Si ratio and Cu”. In: *Corrosion Science* 76 (2013), pp. 119–128. ISSN: 0010938X. DOI: 10.1016/j.corsci.2013.06.035.

[41] Xia Ming Chen, Qi Peng Dong, Zhen Guang Liu, Xiao Nan Wang, Qing Yu Zhang, Zeng Rong Hu, and Hiromi Nagaumi. “Fe-bearing intermetallics transformation and its influence on the corrosion resistance of Al–Mg–Si alloy weld joints”. In: *Journal of Materials Research and Technology* 9.6 (2020), pp. 16116–16125. ISSN: 22387854. DOI: 10.1016/j.jmrt.2020.11.077.

[42] A. Aballe, M. Bethencourt, F. J. Botana, M. J. Cano, and M. Marcos. “Localized alkaline corrosion of alloy AA5083 in neutral 3.5% NaCl solution”. In: *Corrosion Science* 43.9 (2001), pp. 1657–1674. ISSN: 0010938X. DOI: 10.1016/S0010-938X(00)00166-9.

[43] M. Bethencourt, F. J. Botana, J. J. Calvino, M. Marcos, J. Pérez, and M. A. Rodríguez. “The influence of the surface distribution of Al6(MnFe) intermetallic on the electrochemical response of AA5083 aluminium alloy in NaCl solutions”. In: *Materials Science Forum* 289-292.PART 1 (1998), pp. 567–574. ISSN: 16629752. DOI: 10.4028/www.scientific.net/msf.289-292.567.

[44] U. DONATUS, G. E. THOMPSON, J. A. OMOTOYINBO, K. K. ALANEME, S. ARIBO, and O. G. AGBABIAKA. “Corrosion pathways in aluminium alloys”. In: *Transactions of Nonferrous Metals Society of China (English Edition)* 27.1 (2017), pp. 55–62. ISSN: 10036326. DOI: 10.1016/S1003-6326(17)60006-2.

[45] A. Aballe, M. Bethencourt, F. J. Botana, M. Marcos, and J. M. Sánchez-Amaya. "Influence of the degree of polishing of alloy AA 5083 on its behaviour against localised alkaline corrosion". In: *Corrosion Science* 46.8 (2004), pp. 1909–1920. ISSN: 0010938X. DOI: 10.1016/j.corsci.2003.10.028.

[46] Feng Li Zeng, Zhong Ling Wei, Jin Feng Li, Chao Xing Li, Xing Tan, Zhao Zhang, and Zi Qiao Zheng. "Corrosion mechanism associated with Mg 2Si and Si particles in Al-Mg-Si alloys". In: *Transactions of Nonferrous Metals Society of China (English Edition)* 21.12 (2011), pp. 2559–2567. ISSN: 10036326. DOI: 10.1016/S1003-6326(11)61092-3.

[47] V Guillaumin, P Schmutz, and GS Frankel. "Characterization of corrosion interfaces by the scanning Kelvin probe force microscopy technique". In: *Journal of the electrochemical society* 148.5 (2001), B163.

[48] P. Schmutz and G. S. Frankel. "Corrosion Study of AA2024-T3 by Scanning Kelvin Probe Force Microscopy and In Situ Atomic Force Microscopy Scratching". In: *Journal of The Electrochemical Society* 145.7 (July 1998), p. 2295. DOI: 10.1149/1.1838634.

[49] P. Schmutz and G. S. Frankel. "Characterization of AA2024-T3 by Scanning Kelvin Probe Force Microscopy". In: *Journal of The Electrochemical Society* 145.7 (July 1998), p. 2285. DOI: 10.1149/1.1838633.

[50] M Femenia, C Canalias, Jinshan Pan, and Christofer Leygraf. "Scanning Kelvin probe force microscopy and magnetic force microscopy for characterization of duplex stainless steels". In: *Journal of The Electrochemical Society* 150.6 (2003), B274.

[51] Namurata Sathirachinda, Rachel Pettersson, and Jinshan Pan. "Depletion effects at phase boundaries in 2205 duplex stainless steel characterized with SKPFM and TEM/EDS". In: *Corrosion Science* 51.8 (2009), pp. 1850–1860.

[52] Namurata Sathirachinda, Rachel Pettersson, Sten Wessman, Ulf Kivisäkk, and Jinshan Pan. "Scanning Kelvin probe force microscopy study of chromium nitrides in 2507 super duplex stainless steel—Implications and limitations". In: *Electrochimica Acta* 56.4 (2011), pp. 1792–1798.

[53] S Mato, G Alcala, TG Woodcock, A Gebert, J Eckert, and L Schultz. "Corrosion behaviour of a Ti-base nanostructure-dendrite composite". In: *Electrochimica acta* 50.12 (2005), pp. 2461–2467.

[54] Loïc Lacroix, Laurence Ressier, Christine Blanc, and Georges Mankowski. "Combination of AFM, SKPFM, and SIMS to Study the Corrosion Behavior of S-phase particles in AA2024-T351". In: *Journal of The Electrochemical Society* 155.4 (Jan. 2008), p. C131. DOI: 10.1149/1.2833315.

[55] PEPM Campestrini, EPM Van Westing, HW Van Rooijen, and JHW De Wit. "Relation between microstructural aspects of AA2024 and its corrosion behaviour investigated using AFM scanning potential technique". In: *Corrosion science* 42.11 (2000), pp. 1853–1861.

A

[56] Kiryl Yasakau. "Application of AFM-Based Techniques in Studies of Corrosion and Corrosion Inhibition of Metallic Alloys". In: *Corrosion and Materials Degradation* 1.3 (2020), pp. 345–372. ISSN: 2624-5558. DOI: 10.3390/cmd1030017. URL: https://www.mdpi.com/2624-5558/1/3/17.

[57] Wilhelm Melitz, Jian Shen, Andrew C. Kummel, and Sangyeob Lee. "Kelvin probe force microscopy and its application". In: *Surface Science Reports* 66.1 (2011), pp. 1–27. ISSN: 0167-5729. DOI: https://doi.org/10.1016/j.surfrep.2010.10.001.

[58] Allen J Bard and Michael V Mirkin. *Scanning electrochemical microscopy*. CRC Press, 2022. DOI: https://doi.org/10.1201/9781003004592.

[59] Jesse C. Seegmiller and Daniel A. Buttry. "A SECM Study of Heterogeneous Redox Activity at AA2024 Surfaces". In: *Journal of The Electrochemical Society* 150.9 (July 2003), B413. DOI: 10.1149/1.1593041.

[60] C. F. Dong, H. Luo, K. Xiao, X. G. Li, and Y. F. Cheng. "In Situ Characterization of Pitting Corrosion of Stainless Steel by a Scanning Electrochemical Microscopy". In: *Journal of Materials Engineering and Performance* 21 (3 Mar. 2012), pp. 406–410. ISSN: 1059-9495. DOI: 10.1007/s11665-011-9899-y.

[61] A. Davoodi, J. Pan, C. Leygraf, and S. Norgren. "In situ investigation of localized corrosion of aluminum alloys in chloride solution using integrated EC-AFM/SECM techniques". In: *Electrochemical and Solid-State Letters* 8 (6 2005), pp. 21–24. ISSN: 10990062. DOI: 10.1149/1.1911900.

[62] Yuehua Yin, Lin Niu, Min Lu, Weikuan Guo, and Shenhao Chen. "In situ characterization of localized corrosion of stainless steel by scanning electrochemical microscope". In: *Applied Surface Science* 255 (22 Aug. 2009), pp. 9193–9199. ISSN: 01694332. DOI: 10.1016/j.apsusc.2009.07.003.

[63] Y González-Garcıa, G.T Burstein, S González, and R.M Souto. "Imaging metastable pits on austenitic stainless steel in situ at the open-circuit corrosion potential". In: *Electrochemistry Communications* 6 (7 July 2004), pp. 637–642. ISSN: 13882481. DOI: 10.1016/j.elecom.2004.04.018.

[64] Sina S. Jamali, Simon E. Moulton, Dennis E. Tallman, Maria Forsyth, Jan Weber, and Gordon G. Wallace. "Applications of scanning electrochemical microscopy (SECM) for local characterization of AZ31 surface during corrosion in a buffered media". In: *Corrosion Science* 86 (2014), pp. 93–100. ISSN: 0010938X. DOI: 10.1016/j.corsci.2014.04.035.

[65] Decheng Kong, Chaofang Dong, Zhaoran Zheng, Feixiong Mao, Aoni Xu, Xiaoqing Ni, Cheng Man, Jizheng Yao, Kui Xiao, and Xiaogang Li. "Surface monitoring for pitting evolution into uniform corrosion on Cu-Ni-Zn ternary alloy in alkaline chloride solution: ex-situ LCM and in-situ SECM". In: *Applied Surface Science* 440 (May 2018), pp. 245–257. ISSN: 01694332. DOI: 10.1016/j.apsusc.2018.01.116.

[66] Chuan He, Wen Feng Mo, Ya Ya Zheng, S. P. Feng, and Bing Hui Luo. "A SECM study of redox activity on Al-Mg-Si alloy in organic/aqueous solution". In: *Journal of Alloys and Compounds* 888 (2021), p. 161596. ISSN: 09258388. DOI: 10.1016/j.jallcom.2021.161596.

[67] Zhenni Ye, Zejie Zhu, Qinhao Zhang, Xiaoyan Liu, Jianqing Zhang, and Fahe Cao. "In situ SECM mapping of pitting corrosion in stainless steel using submicron Pt ultramicroelectrode and quantitative spatial resolution analysis". In: *Corrosion Science* 143 (February 2018), pp. 221–228. ISSN: 0010938X. DOI: 10.1016/j.corsci.2018.08.014.

[68] David Polcari, Philippe Dauphin-Ducharme, and Janine Mauzeroll. "Scanning Electrochemical Microscopy: A Comprehensive Review of Experimental Parameters from 1989 to 2015". In: *Chemical Reviews* 116 (22 2016), pp. 13234–13278. ISSN: 15206890. DOI: 10.1021/acs.chemrev.6b00067.

[69] Y. González-García, J.M.C Mol, T. Muselle, I. De Graeve, G. Van Assche, G. Scheltjens, B. Van Mele, and H. Terryn. "SECM study of defect repair in self-healing polymer coatings on metals". In: *Electrochemistry Communications* 13.2 (2011), pp. 169–173. ISSN: 1388-2481. DOI: https://doi.org/10.1016/j.elecom.2010.12.005.

[70] Yaiza González-García, Juan José Santana, Jorge González-Guzmán, Javier Izquierdo, Sergio González, and Ricardo M. Souto. "Scanning electrochemical microscopy for the investigation of localized degradation processes in coated metals". In: *Progress in Organic Coatings* 69.2 (2010). Special Issue on The Sixth International Workshop on "Application of Electrochemical Techniques to Organic Coatings (AETOC)", pp. 110–117. ISSN: 0300-9440. DOI: https://doi.org/10.1016/j.porgcoat.2010.04.006.

[71] Ayodele O. Okunola, Tharamani Chikka Nagaiah, Xingxing Chen, Kathrin Eckhard, Wolfgang Schuhmann, and Michael Bron. "Visualization of local electrocatalytic activity of metalloporphyrins towards oxygen reduction by means of redox competition scanning electrochemical microscopy (RC-SECM)". In: *Electrochimica Acta* 54.22 (2009), pp. 4971–4978. ISSN: 0013-4686. DOI: https://doi.org/10.1016/j.electacta.2009.02.047.

[72] Woo-Jin Lee and Su-Il Pyun. "Effects of sulphate ion additives on the pitting corrosion of pure aluminium in 0.01 M NaCl solution". In: *Electrochimica Acta* 45.12 (2000), pp. 1901–1910. ISSN: 0013-4686. DOI: https://doi.org/10.1016/S0013-4686(99)00418-1.

[73] Su-Il Pyun and Sung-Mo Moon. "The inhibition mechanism of pitting corrosion of pure aluminum by nitrate and sulfate ions in neutral chloride solution". In: *Journal of Solid State Electrochemistry* 3.6 (1999), pp. 331–336.

[74] W.J. Rudd and J.C. Scully. "The function of the repassivation process in the inhibition of pitting corrosion on aluminium". In: *Corrosion Science* 20.5 (1980), pp. 611–631. ISSN: 0010-938X. DOI: https://doi.org/10.1016/0010-938X(80)90098-0.

[75] G.S. Chen, M. Gao, and R.P. Wei. "Microconstituent-Induced Pitting Corrosion in Aluminum Alloy 2024-T3". In: *Corrosion* 52.01 (Jan. 1996). ISSN: 0010-9312. eprint: https://onepetro.org/corrosion/article-pdf/2184597/nace-96010008.pdf.

[76] V. Annamalai, J.B. Hiskey, and L.E. Murr. “The effects of kinetic variables on the structure of copper deposits cemented on pure aluminum discs: A scanning electron microscopic study”. In: *Hydrometallurgy* 3.2 (1978), pp. 163–180. ISSN: 0304-386X. DOI: https://doi.org/10.1016/0304-386X(78)90018-X.

[77] HM Obispo, LE Murr, RM Arrowood, and EA Trillo. “Copper deposition during the corrosion of aluminum alloy 2024 in sodium chloride solutions”. In: *Journal of Materials Science* 35.14 (2000), pp. 3479–3495.

[78] Tiago Ferreira and Wayne Rasband. “ImageJ user guide”. In: *ImageJ/Fiji* 1 (2012), pp. 155–161.

[79] Z Szklarska-Smialowska. “Pitting corrosion of aluminum”. In: *Corrosion Science* 41.9 (1999), pp. 1743–1767. ISSN: 0010-938X. DOI: https://doi.org/10.1016/S0010-938X(99)00012-8.

[80] Rama B. Inturi and Z. Szklarska-Smialowska. “Dependence of the pitting potential of Al alloys on solubility of alloying element oxides”. In: *Corrosion Science* 34.4 (1993), pp. 705–710. ISSN: 0010-938X. DOI: https://doi.org/10.1016/0010-938X(93)90282-L.

[81] G. S. Frankel, M. A. Russak, C. V. Jahnes, M. Mirzamaani, and V. A. Brusic. “Pitting of Sputtered Aluminum Alloy Thin Films”. In: *Journal of The Electrochemical Society* 136.4 (Apr. 1989), p. 1243. DOI: 10.1149/1.2096864.

[82] B. A. Shaw, G. D. Davis, T. L. Fritz, B. J. Rees, and W. C. Moshier. “The Influence of Tungsten Alloying Additions on the Passivity of Aluminum”. In: *Journal of The Electrochemical Society* 138.11 (Nov. 1991), p. 3288. DOI: 10.1149/1.2085404.

[83] Mary Katherine Cavanaugh. “Modeling the environmental dependence of localized corrosion evolution in AA7075-T651”. PhD thesis. The Ohio State University, 2009.